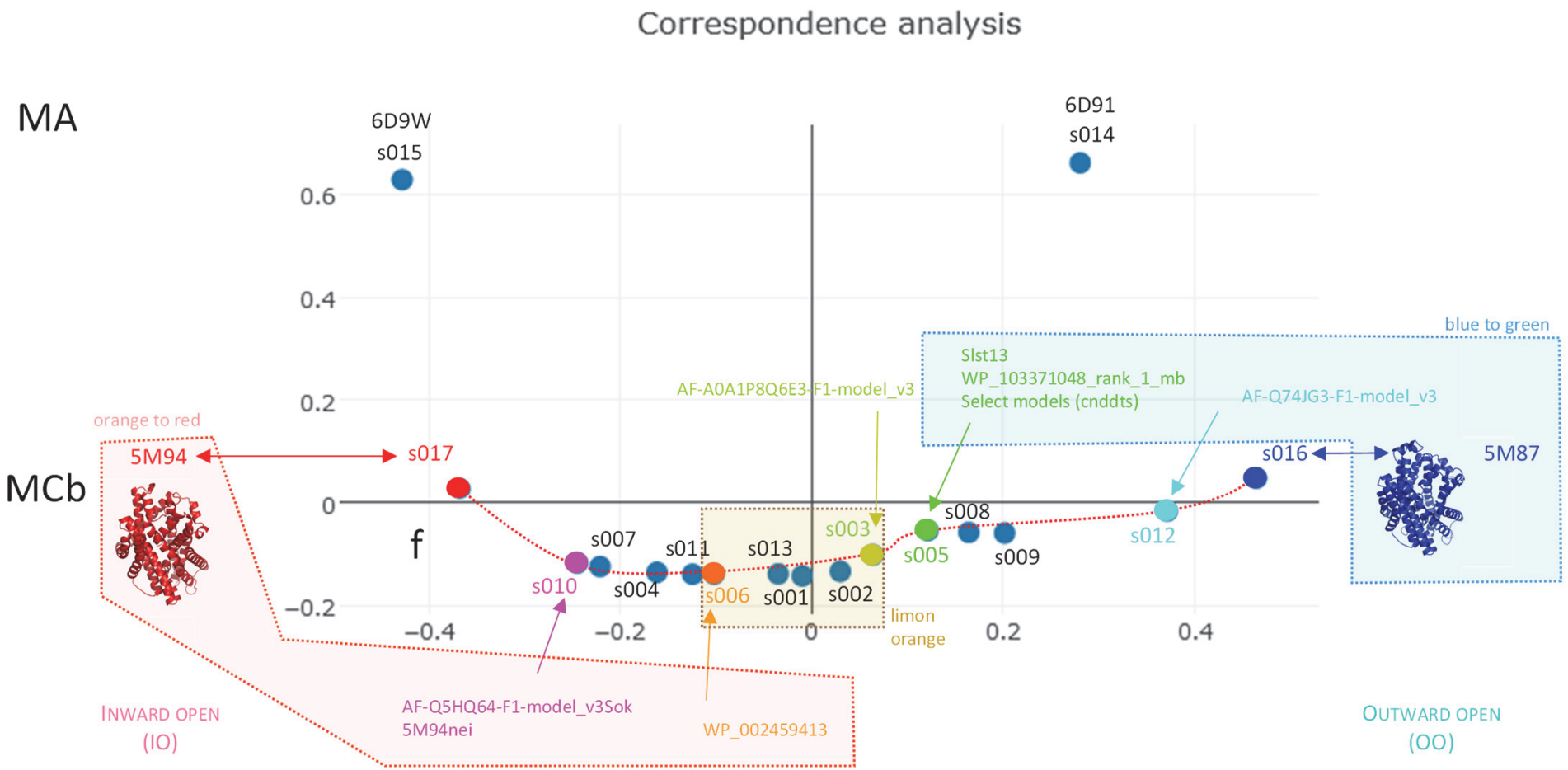

Figure S1. AF2/CF modeling of various MCb predicts a series of possible conformers in carrier cycle. A suite of candidate conformers populating the hypothetical path linking solved 3D structures of MCb in outward open (OO, 5M87) and inward open (IO, 5M94) states was selected based on Dali 'all against all' 3D comparisons using MCb PDB structures as reference points (and equivalent MA structures as outgroup). The 5 selected models segregate with either OO (cyan, green) or IO (magenta, orange) MCb reference structure, or neither (limon). They were binned in separate groups (blue to green ensemble, limon-orange pair, orange to red ensemble) to examine how communities of networked residues evolve during MCb OO to IO transition.

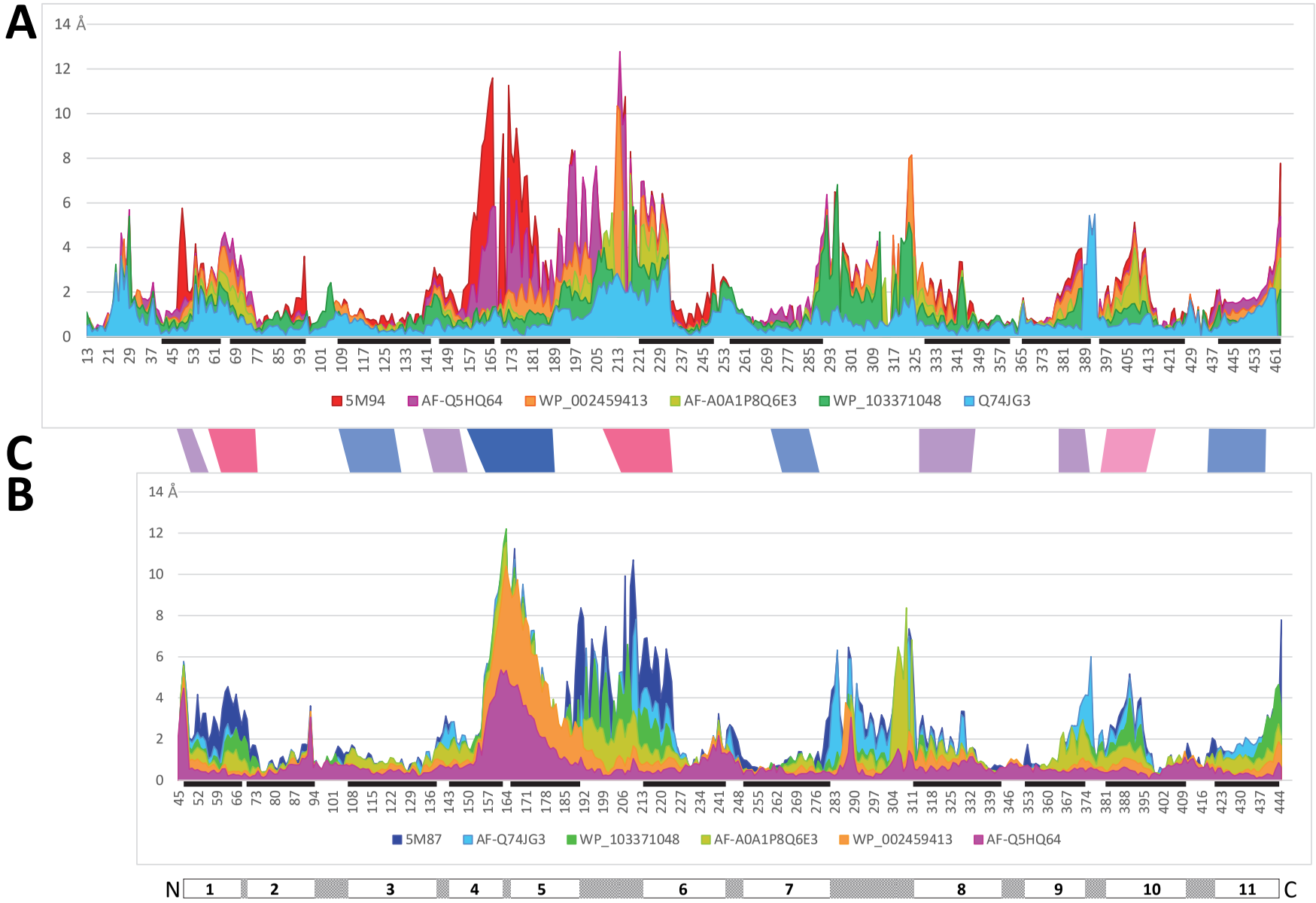

Figure S2. Per residue RMSD of AF2/CF MCb models relative to both MCb reference structures for each candidate conformer selected. Per residue Ca RMSD profiles (in Angstroms) were deduced from pairwise structural alignments onto OO *(*5M87, **A***)* and IO (5M94, **B**) MCb structures, whose respective positions of transmembrane helices 1-11 is indicated below. Progression of local structural changes that occur early (cyan, green) vs late (orange, magenta) during the OO to IO transition suggests tentative ordering of the possible intramolecular rearrangements taking place (**C**, red to blue).

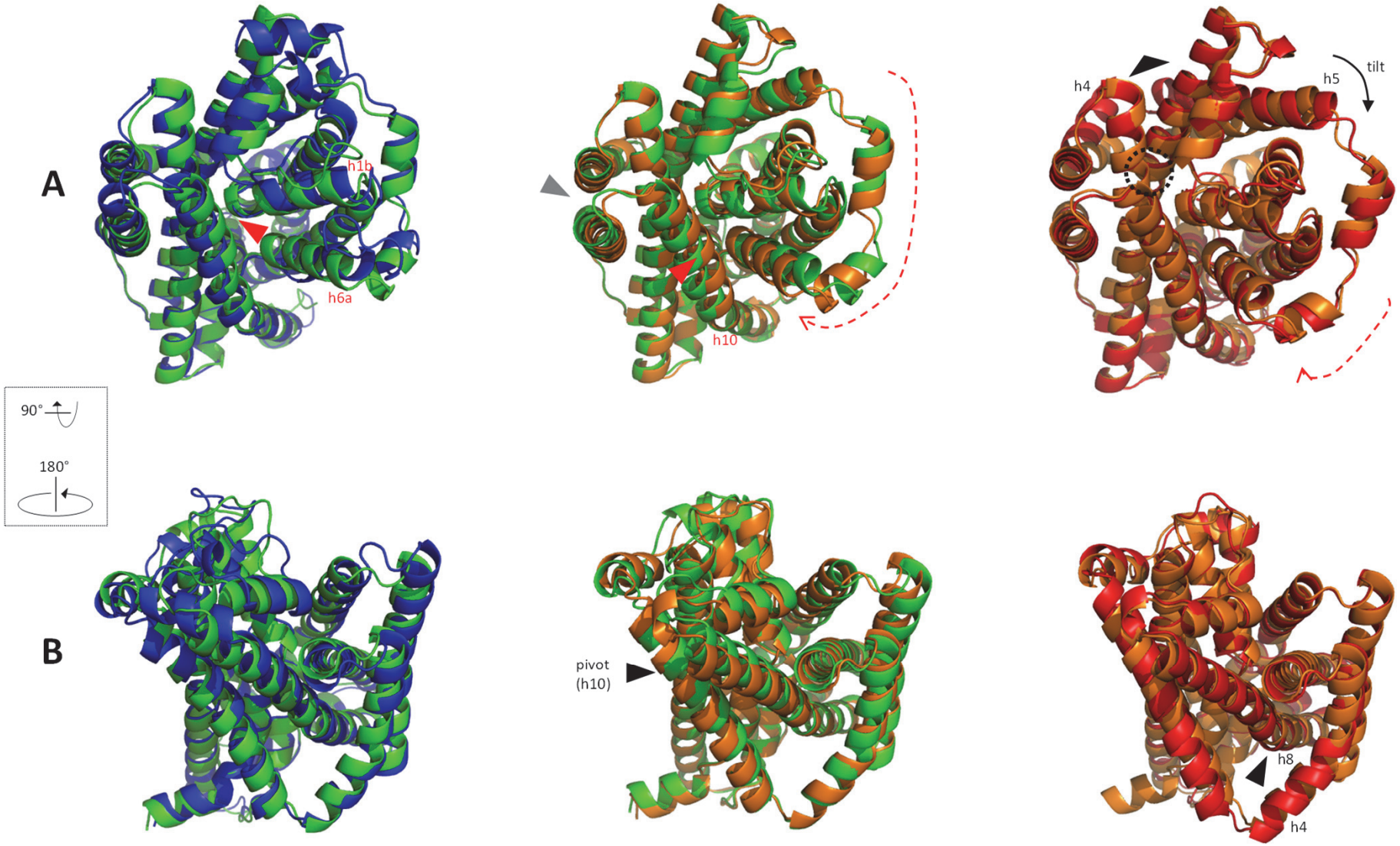

Figure S3. Progression in predicted intramolecular rearrangements during MCb OO to IO transition.
Multiple superposition (POSA) of two reference 3D structures (OO 5M87 blue and IO 5M94 red) with two CF pdb models (green, orange) shows intramolecular rearrangements that mimic Me^{2+} binding to (*Left*), and occlusion of (*Middle*), the external substrate binding site before opening of the inner gate (*Right*). Alternate views are presented from the cell exterior (**A**) and within the membrane (**B**).

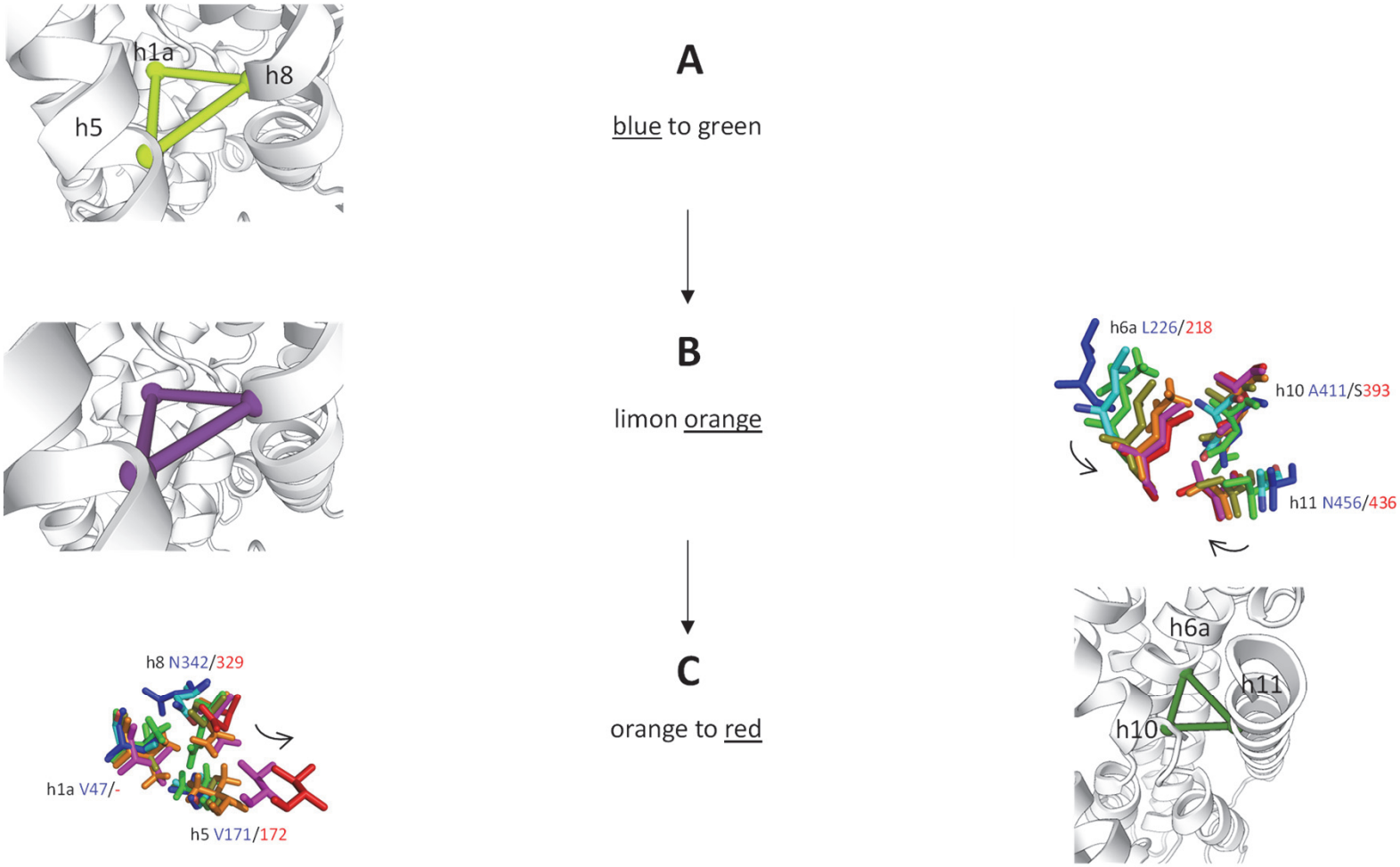

Figure S4. Alternate communities of networked residues distinguish MCb OO from IO states. *Left panel*. h8 N342/329 (5M87/5M94) is part of a small network connecting to h1a and h5. This network holds during initial progression of OO states (blue to green, cf Figure S1, **A**); it evolves during intermediate steps of conformational exchange between OO and IO states (limon and orange, **B**) before disruption, by subsequent displacement of h5 while advancing through IO states (magenta and red, **C**). *Right panel*. Another small network on the opposite side of the molecule connects only in later steps of OO to IO transition, i.e., terminating the conformation switch (post-limon intermediate, **C**).

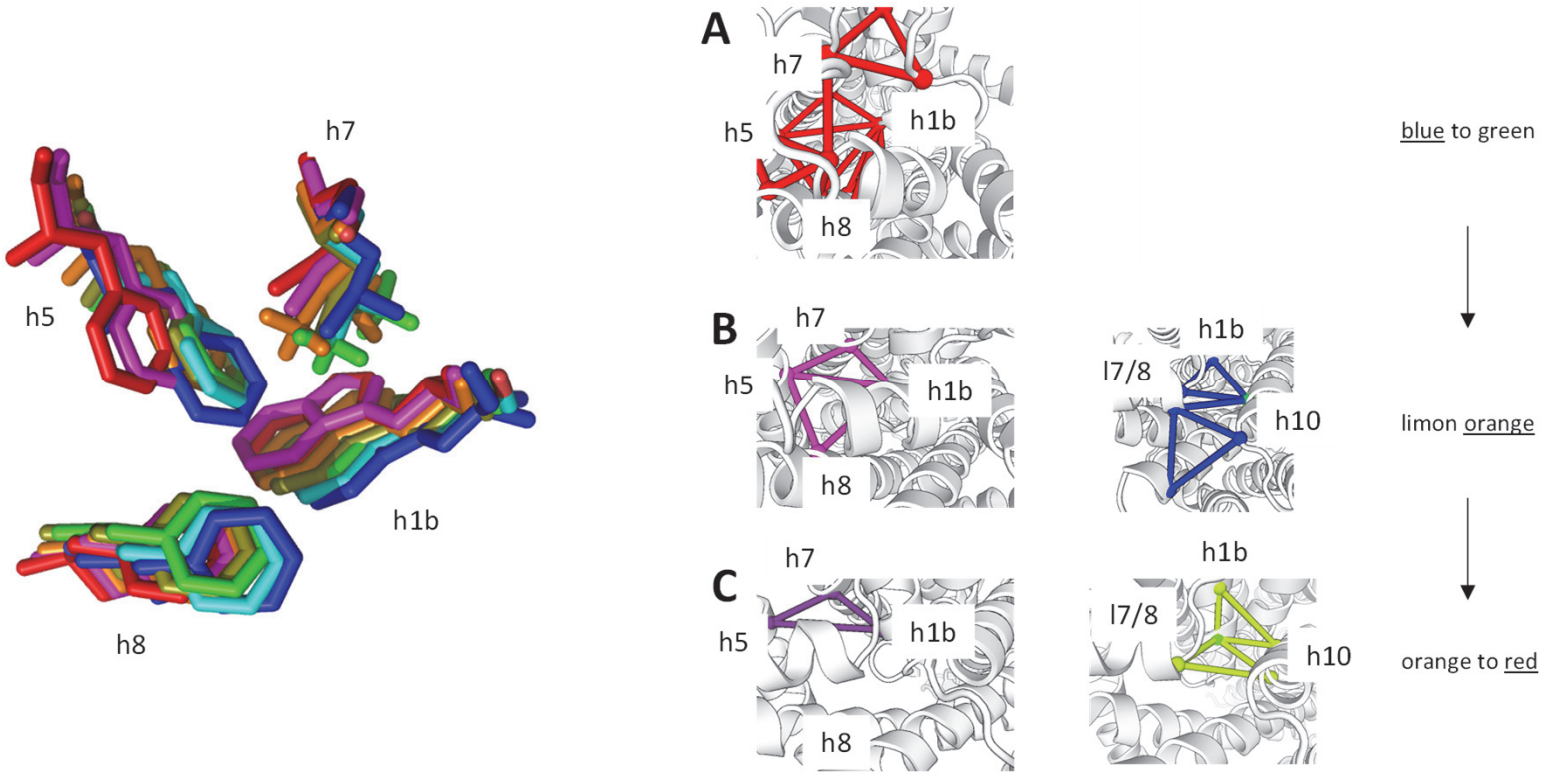

Figure S5. Community of hydrophobic residues evolving during MCb transition from OO to IO states. *Left panel.* Relative side chain orientation and position of the four-residue community linking h1b, h5, h7 and h8. *Right panel.* **A**. This community is part of a larger network through the ensemble of blue to green OO models. **B**. The four-residue community is maintained in the pair of limon-orange models together with neo connections linking h1b to I7/8 and h10. **C**. Only three residues remain connected in the ensemble of orange to red IO models (minus h8 F) also with additional connections between h1b, l7/8 and h10.

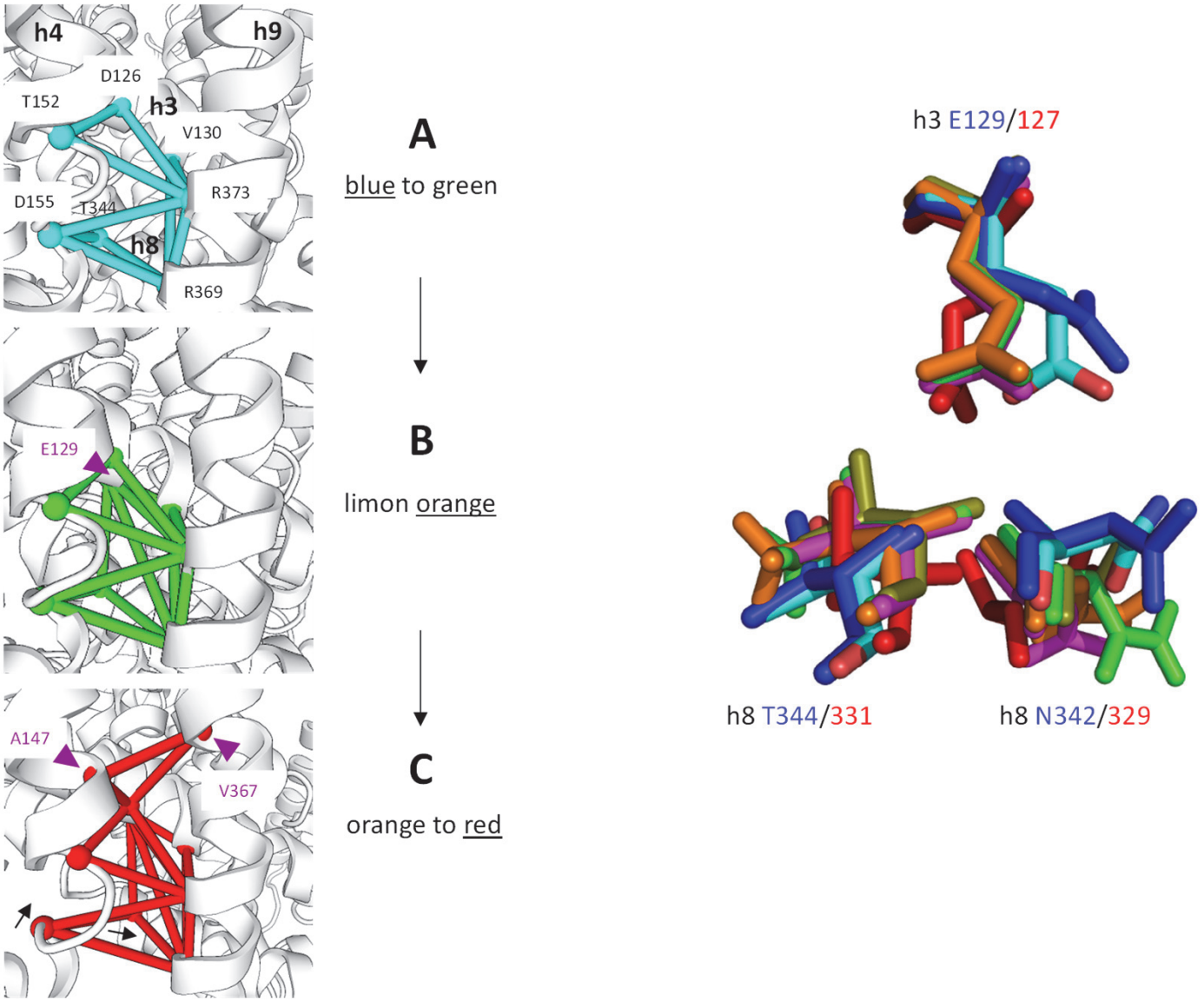

Figure S6. MCb H⁺-network evolves during OO to IO conformation switch. *Left panel*. h3 E129/127 (5M87/5M94) is connected to the H^+ network (including h8 T344/331) in the limon intermediate model (**A**, **B**). Topological reorganization of this network between h4 and h9 later coincides with inner gate opening (ensemble of orange to red models, black arrows, **C**). *Right panel*. h8 N342/329 seems continuously moving throughout carrier OO to IO transition (cf per residue RMSD plots, Figure S2) and remains connected to h1a and h5 until late OO steps (Figure S4, left panel).

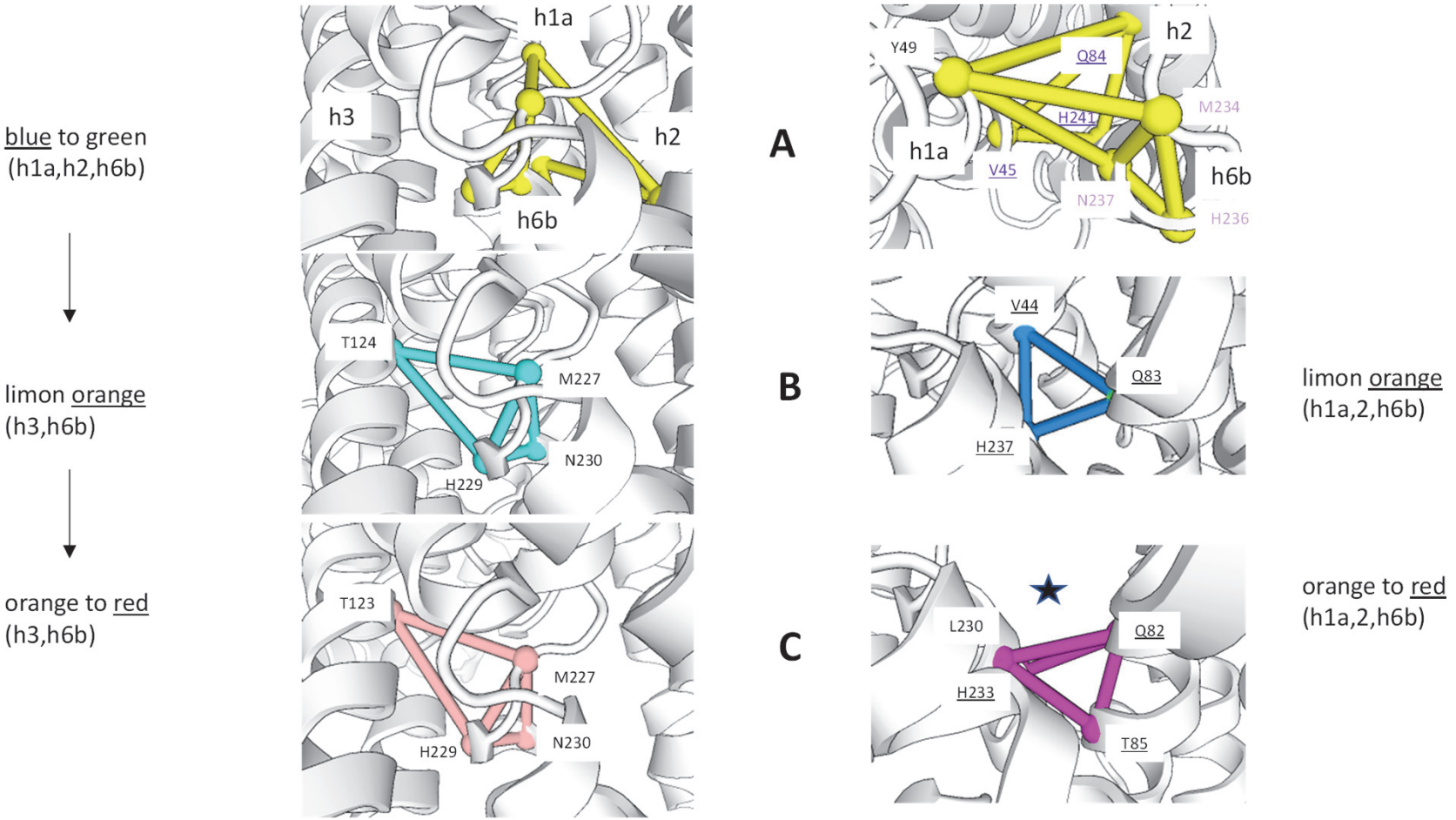

Figure S7. Alternate h6b connections during MCb OO to IO conformation switch. **A**. In OO states (blue to green model ensemble) h6b and h1a are connected both at their top and bottom (cf right panel). **B**, **C**. This community of networked residues splits in two during OO to IO conformation switch (pair of limon orange models). A star marks the absence of h1a from 5M94 structure (**C**).

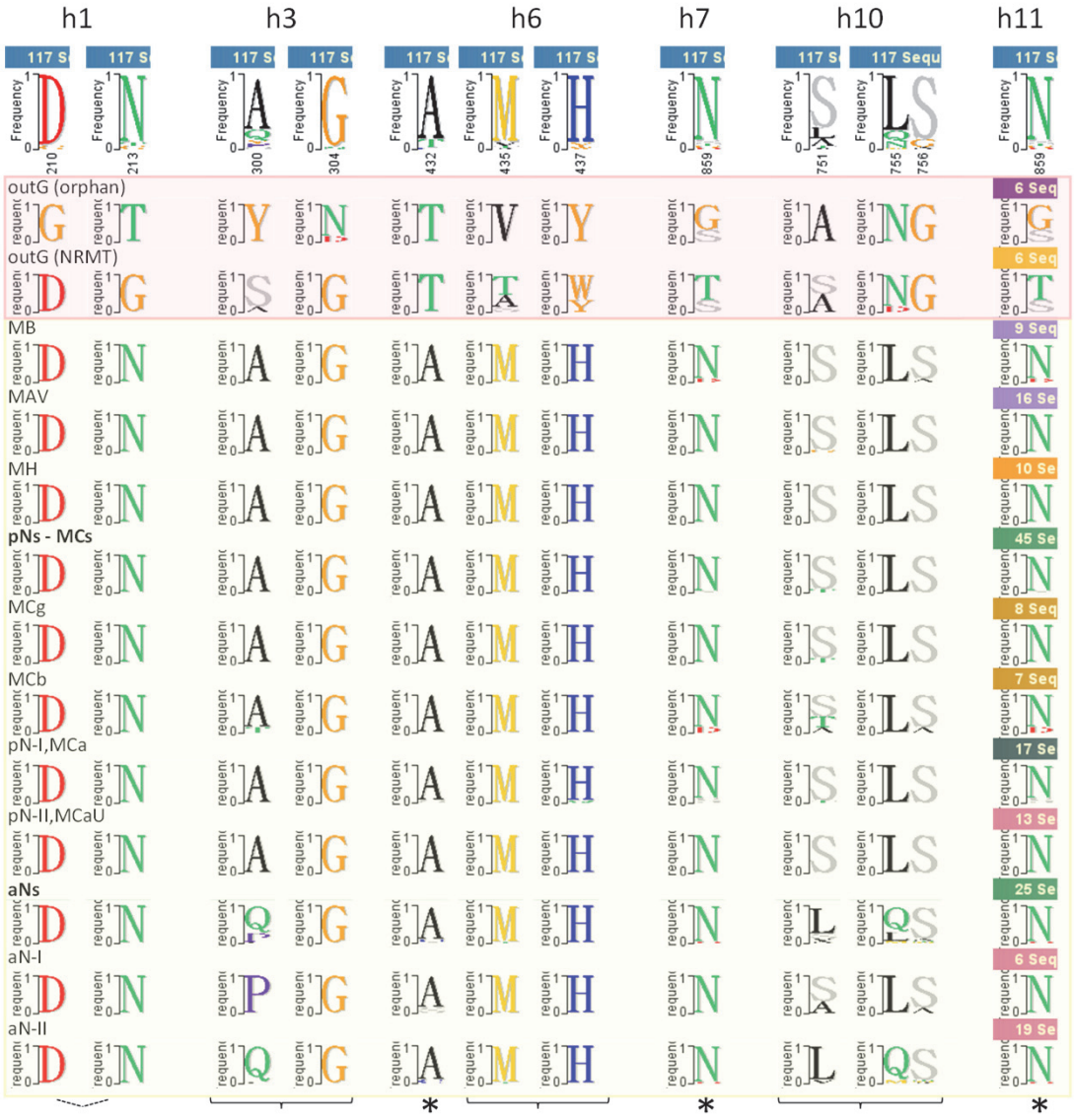

Figure S8. Synapomorphy distinguishing the Slc11 family from phylogenetic outgroups (all part of PFAM01566). The consensus for each clade of the Slc11 family tree (cf Figure 1) is shown for each site representing a type ii evolutionary rate shift between the orphan outgroup and Slc11 carriers. The five combinations of site-directed mutations that were assayed are indicated below: Slc11-specific residues were exchanged for the corresponding outG (orphan/NRMT) residues to study the impact of these evolutionary rate-shifts on AF2/CF modeling of Slc11 conformers using both MCb and MCg1 templates.

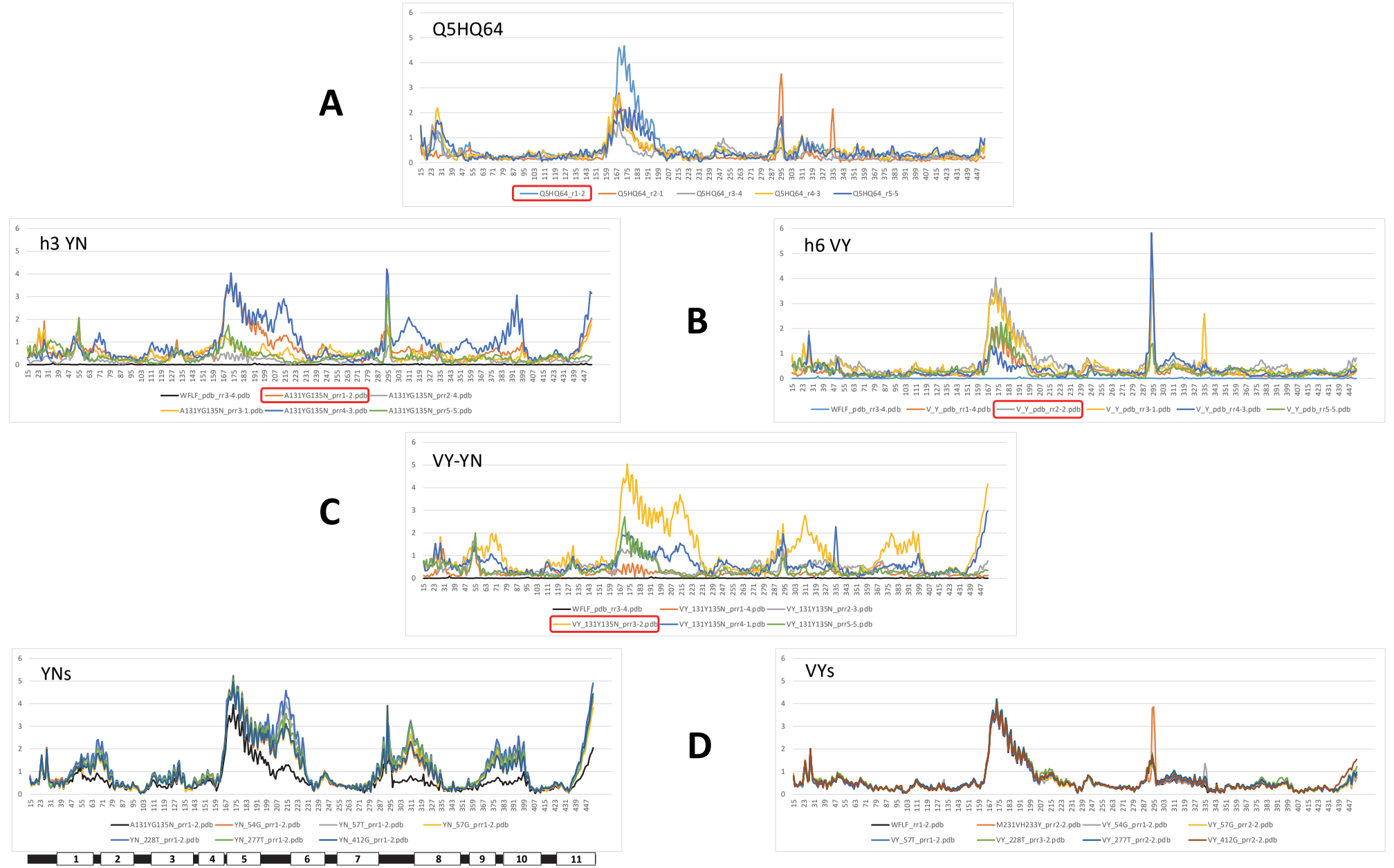

Figure S9. Choice of AF2 trained model2 output (of CF modeling with pdb template) for MCb Q5HQ64 mutagenesis study. **A**. Per residue RMSD of 5 Q5HQ64 CF pdb models each structurally aligned with AF2 Q5HQ64 reference model. Model2, highlighted in red, ranks 1 and appears prone to locally rearrange wt Q5HQ64, with limited inner gate (h4/h5) opening compared to AF2 reference IO model; Model4 was chosen as baseline reference for subsequent pairwise alignment of mutant Q5HQ64 models. **B-D**. Per residue RMSD of CF pdb models for various Q5HQ64 mutants structurally aligned onto native Model4. 5 CF pdb models per mutant: h3 YN (A131Y, G135N) or h6 VY (M231V, H233Y) (**B**), h3 YN h6 VY (**C**), with model2 highlighted in red. CF pdb model2 for compound mutants combining h3 YN or h6 VY with point mutations in helices h1 (D54G, N57T, N57G), h6 (A228T), h7 (N277T) and h11 (N442G) (**D**). None of the latter mutations in h1, h6, h7 or h11 was sufficient alone to induce broad scale change in RMSD (data not shown #2).

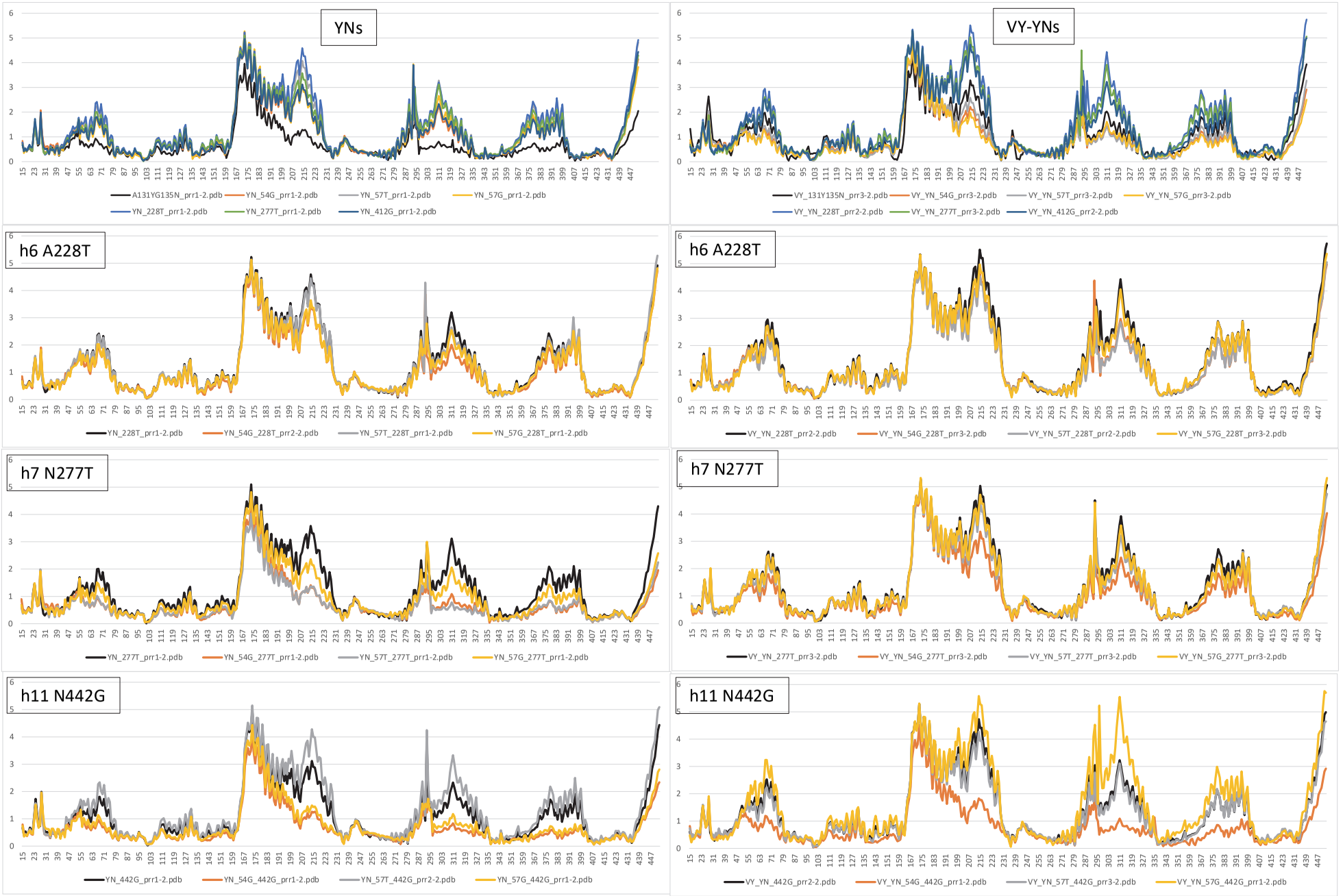

Figure S10. Conformational response to h1 Me^{2+} BS point mutations depends on Q5HQ64 genetic background. Per residue RMSD of Q5HQ64 mutants CF pdb model2 structurally aligned with wt Q5HQ64 CF pdb model4. None of the mutation tested individually influence wt Q5HQ64 conformation (data not shown #2). In YN background (*Left panel*) all mutations tested cooperate with YN, producing broad scale deviation (top), while the impact of h1 mutations (D54G, N57T and N57G) depends on other mutations in h6 (A228T), h7 (N277T) or h11 (N442G). In VY YN background (*Right panel*) h1 mutations limit overall deviation (top); yet their effect is minimal in the presence of h6 A228T, which produces maximal deviation, while D54G has negative impact in the presence of h7 N277T (mild) or h11 N412G (strong).

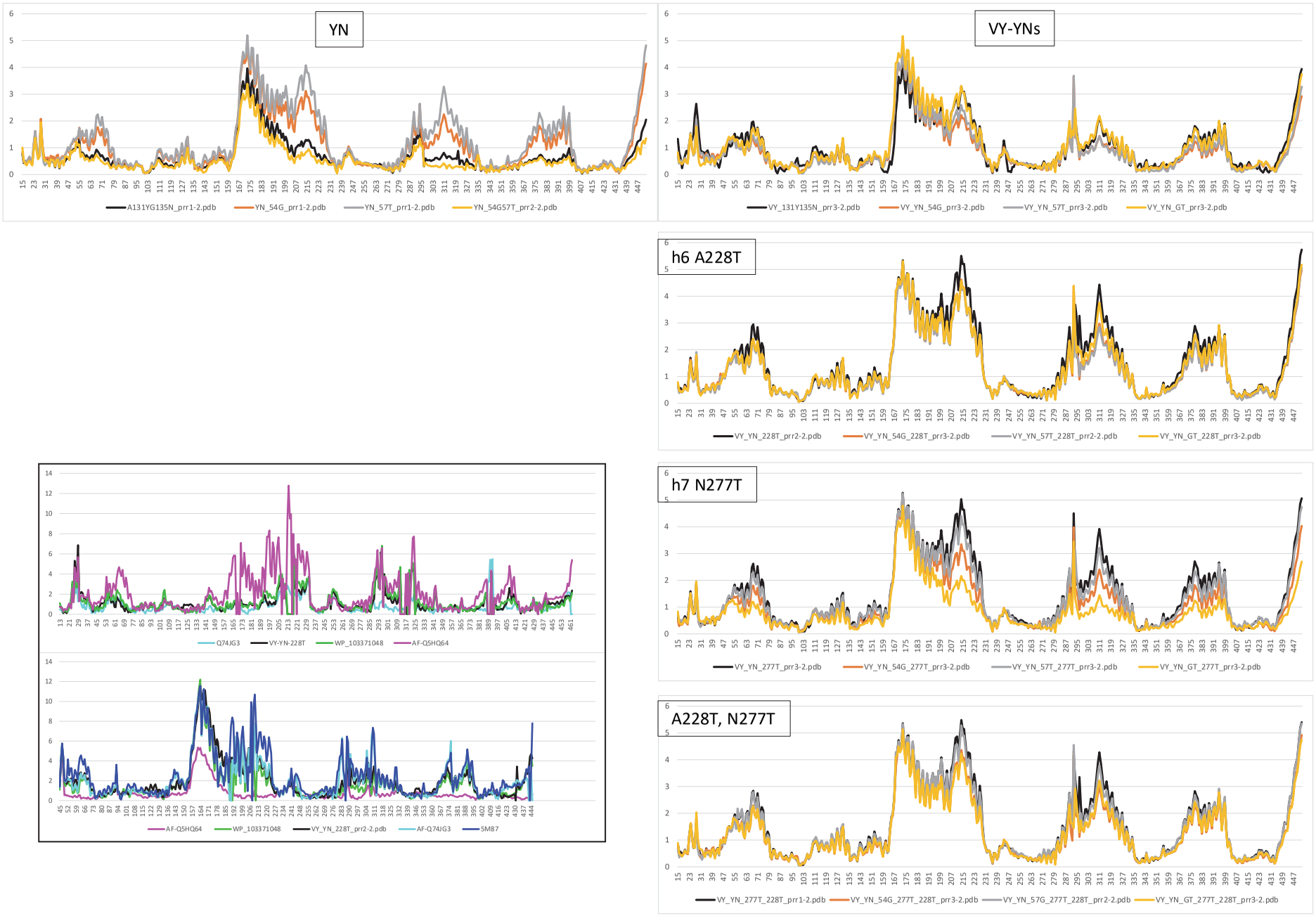

Figure S11. Mutations of Q5HQ64 h1a and h1b Me^{2+} BS have interdependent effects. *Left panel*. In h3 YN background, h1 D54G N57T dual mutation abrogates the cooperative effect of each of h1 mutation taken separately. *Right panel*. In h3 YN h6 VY background, h1 D54G N57T dual mutation has more positive effect than each mutation taken separately (top); it has minimal impact in the presence of h6 A228T background and exerts counter productive interaction with h7 N277T that is compensated by h6 A228T. *Inset*: Per residue RMSD of Q5HQ64 VY YN 228T (VNT) mutant compared to select AF2/CF MCb models (cf SupMat2) relative to both MCb reference structures (OO 5M87, top, and IO 5M94, bottom).

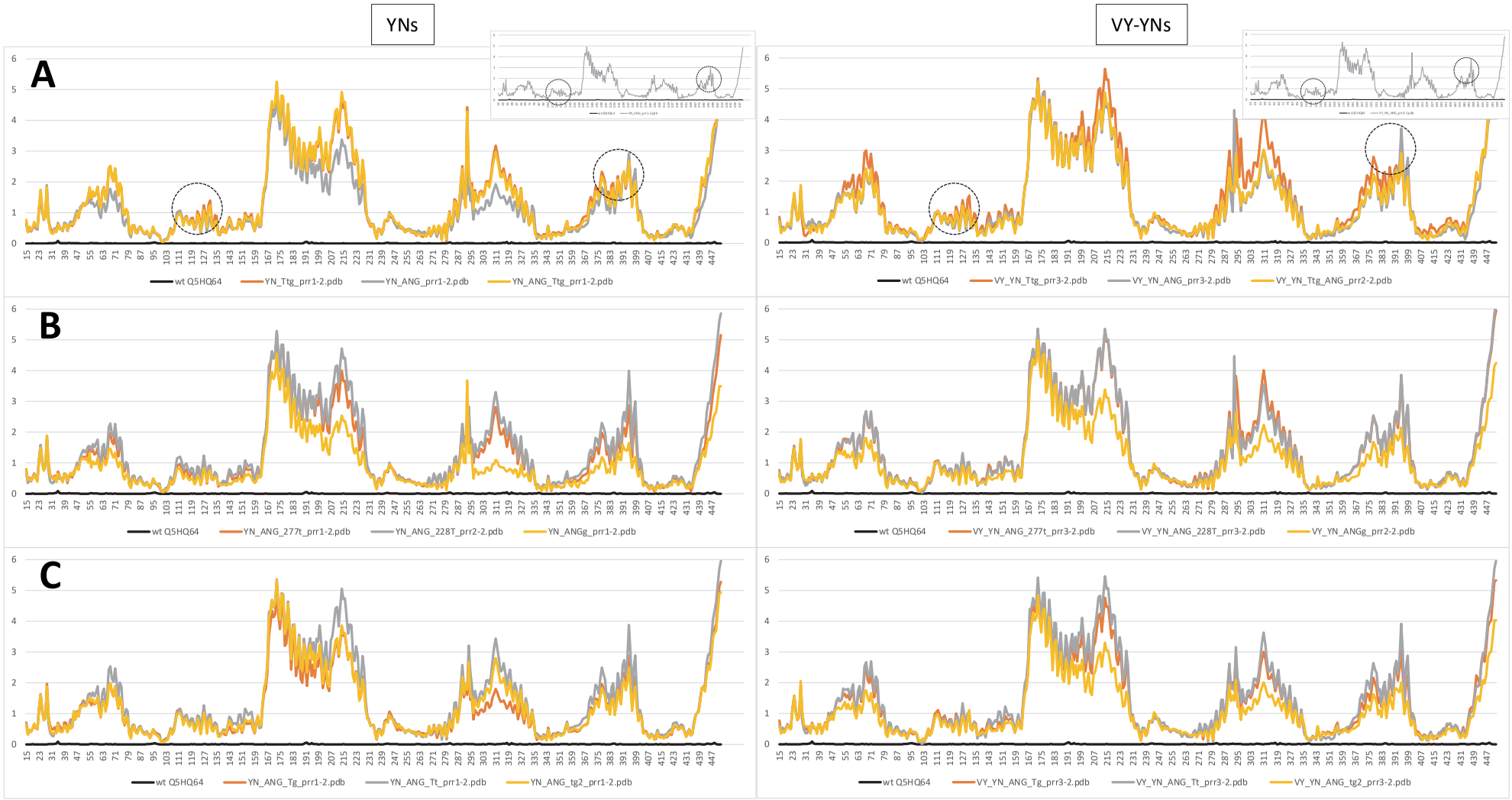

Figure S12. Evidence for direct interaction between MCb Q5HQ64 h3 and h10. Similar mutation combinations were tested both in YN background (*Left panel*) and VY YN background (*Right panel*). Neither h10 ANG nor the triple mutation Ttg were sufficient alone to produce broad scale deviation (data not shown #2). **A**. Effect of h10 triple mutation ANG (S393A L397N S398G, detailed in *insets*) compared to and combined with the triple mutation Ttg (h6 A228T, h7 N277T, h11 N442G). Circles indicate the location of h3 h10 inter helix contacts. **B**. h10 ANG combined to either h6 A228T, h7 N277T or h11 N442G. **C**. h10 ANG combined with either h6 A228T h11 N442G, h6 A228T h7 N277T or h7 N277T h11 N442G. (Baseline, re-run of wt Q5HQ64, model4).

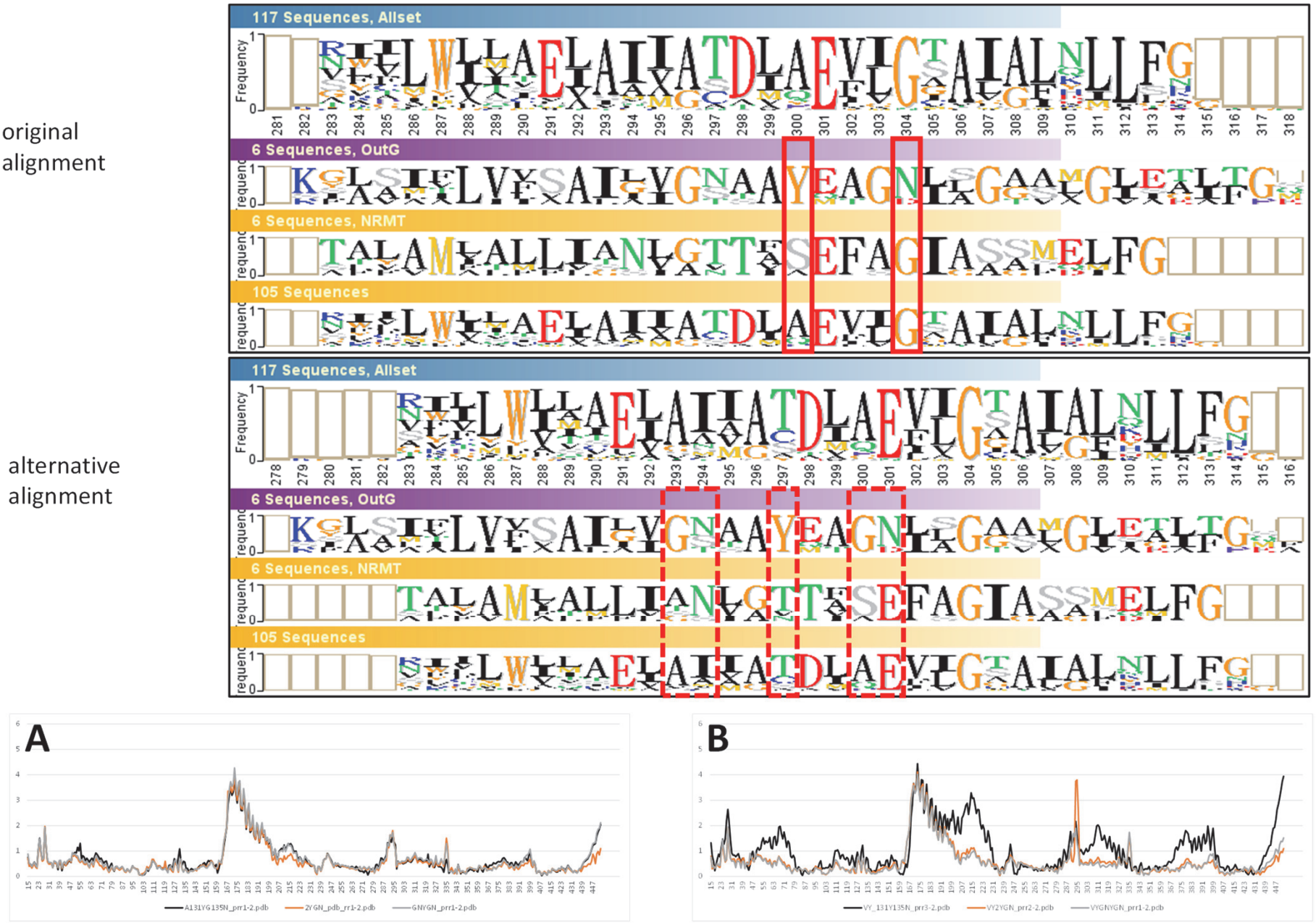

Figure S13. Testing h3 multiple sequence alignment and deduced selection of targeted sites for mutagenesis. *Top panel*. Comparison of alternative h3 alignments and deduced type ii evolutionary rate shifts targeted for mutagenesis (highlighted). The original h3 alignment was used to establish Slc11 phylogeny (cf Figure 1) and the alternative h3 alignment results from sliding both Slc11 and NRMT sequences to the right (+3). Bottom panel. Two combinations of mutations deduced from sites identified with the alternate alignment, h3 ----Y--GN and h3 GN--Y--GN, were introduced in Q5HQ64, either alone (**A**) or in combination with h6 VY (**B**) prior to CF pdb modeling and structural alignment with CF pdb model4.

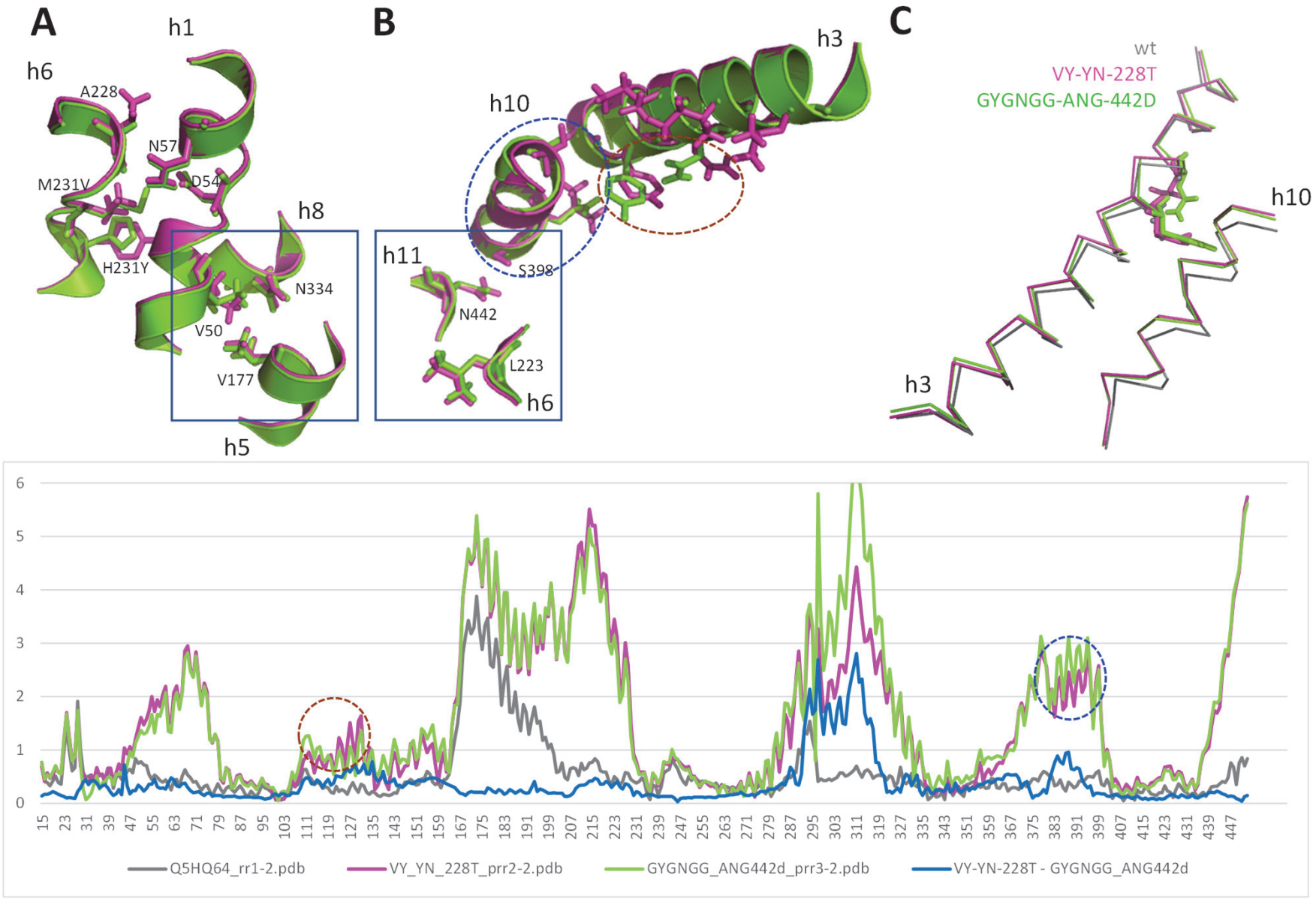

Figure S14. Accommodation of h3 YN mutation in Q5HQ64 compound mutants VY YN 228T and GYGNGG ANG N442D. *Top panel*. **A**. VY YN 228T and GYGNGG AND 442D mutants display superposable arrangements of the Me^{2+} BS and the OO-specific 5M87 community 7 of networked residues (boxed). **B**. The IO-specific 5M94 community 11 [nc18] of connected residues (boxed) also appears superposable while residue side chains in the h3 h10 contact area deviate. **C**. h3 h10 contact area. *Bottom panel*. Per residue RMSD of wt Q5HQ64, VY YN 228T and GYGNGG AND 442D mutants. The blue line shows pairwise deviation between VY-YN-228T and GYGNGG-ANG-442D models.

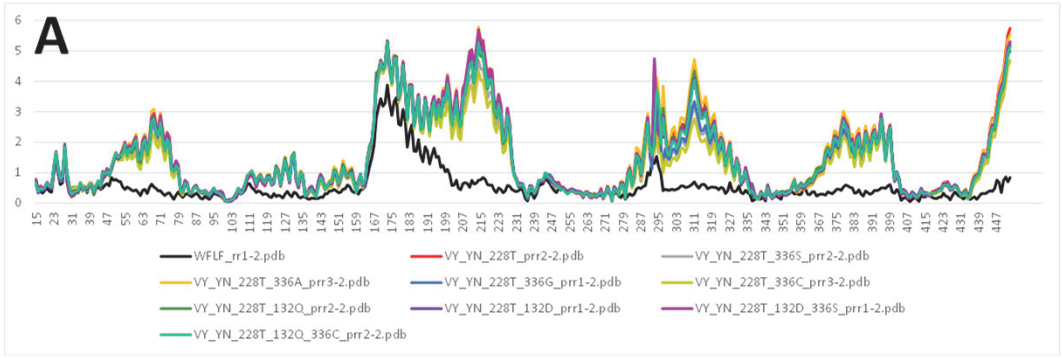

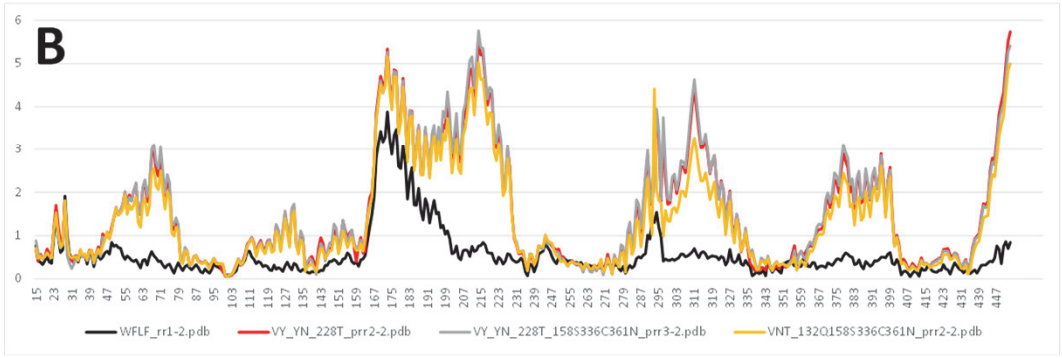

Figure S15. Effect of mutations targeting Slc11 H⁺-network on CF pdb modeling of Q5HQ64 VNT (VY YN A228T) mutant. **A**. Multiple substitutions of h8 T336 and h3 E132 alone or combined. **B**. Compound mutant h3 E132Q h8 T336C h9 R361N with or without h4 D158S. **C**. Natural evolutionary variation of each of the targeted sites.

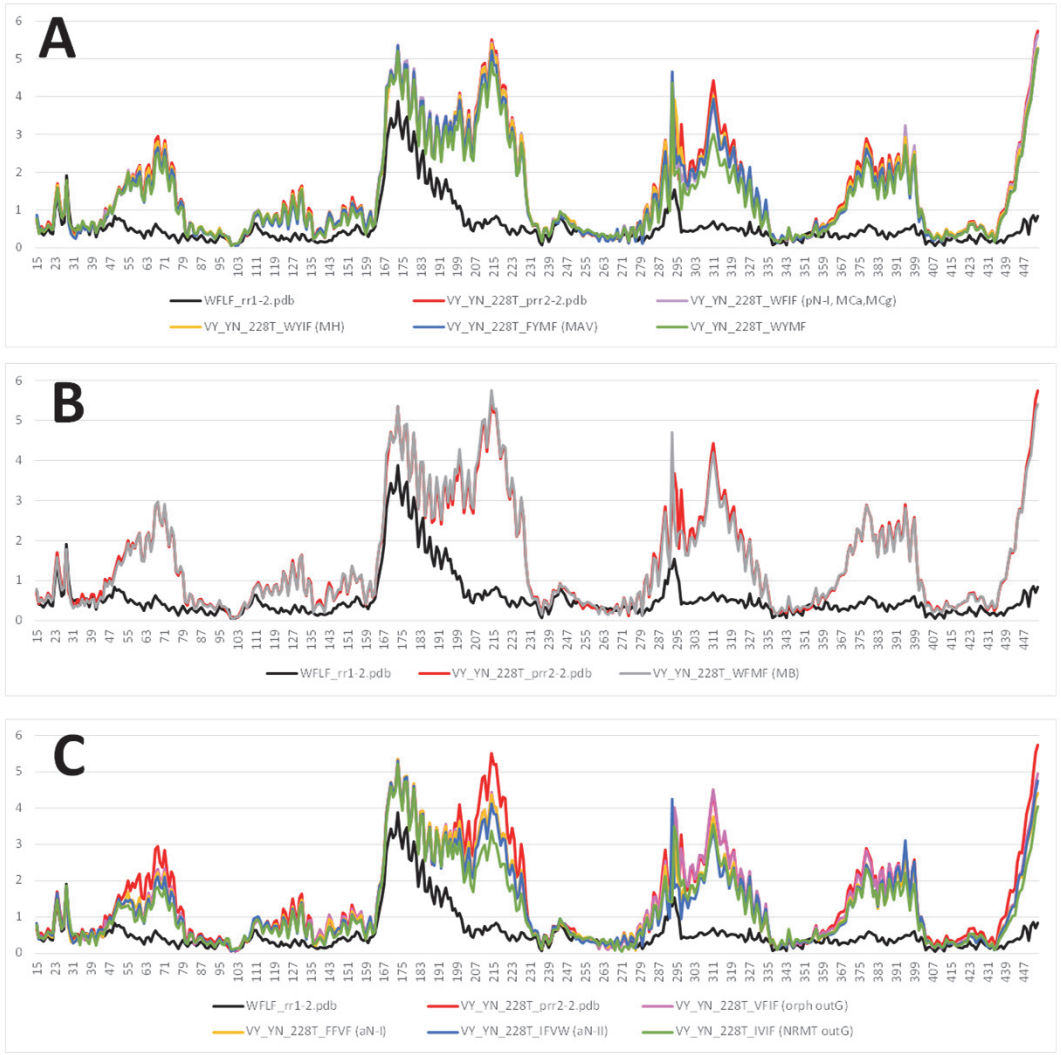

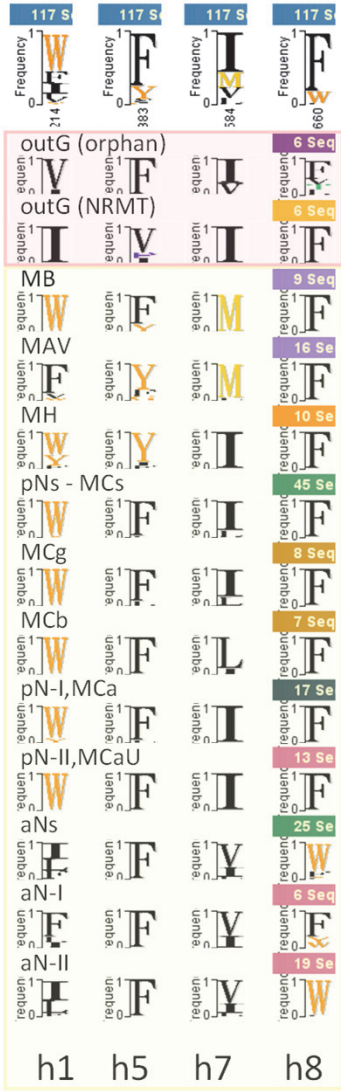

Figure S16. Interaction of h1b, h5, h7 and h8 may regulate coordinated motion of h1b-l1/2 and h6a in Q5HQ64 VY YN A228T. *Left panel.* Influence of mutations mimicking Slc11 clade selective consensus residue combinations on CF pdb modeling of Q5HQ64 VNT mutant. **A**. Consensus sequence for pN-I, MCa and MCg (WFIF); MH (WYIF); MA, MAV (FYMF) plus additional mutant WYMF. **B**. Consensus sequence for MB (WFMF). **C**. Consensus sequence for orphan outgroup (VFIF), NRMT outgroup (IVIF), aN-I (FFVF) and aN-II (IFVW). *Right panel*. Natural evolutionary variation of the targeted sites (i.e., Q5HQ64 h1 W58, h5 F188, h7 L280 and h8 F324).

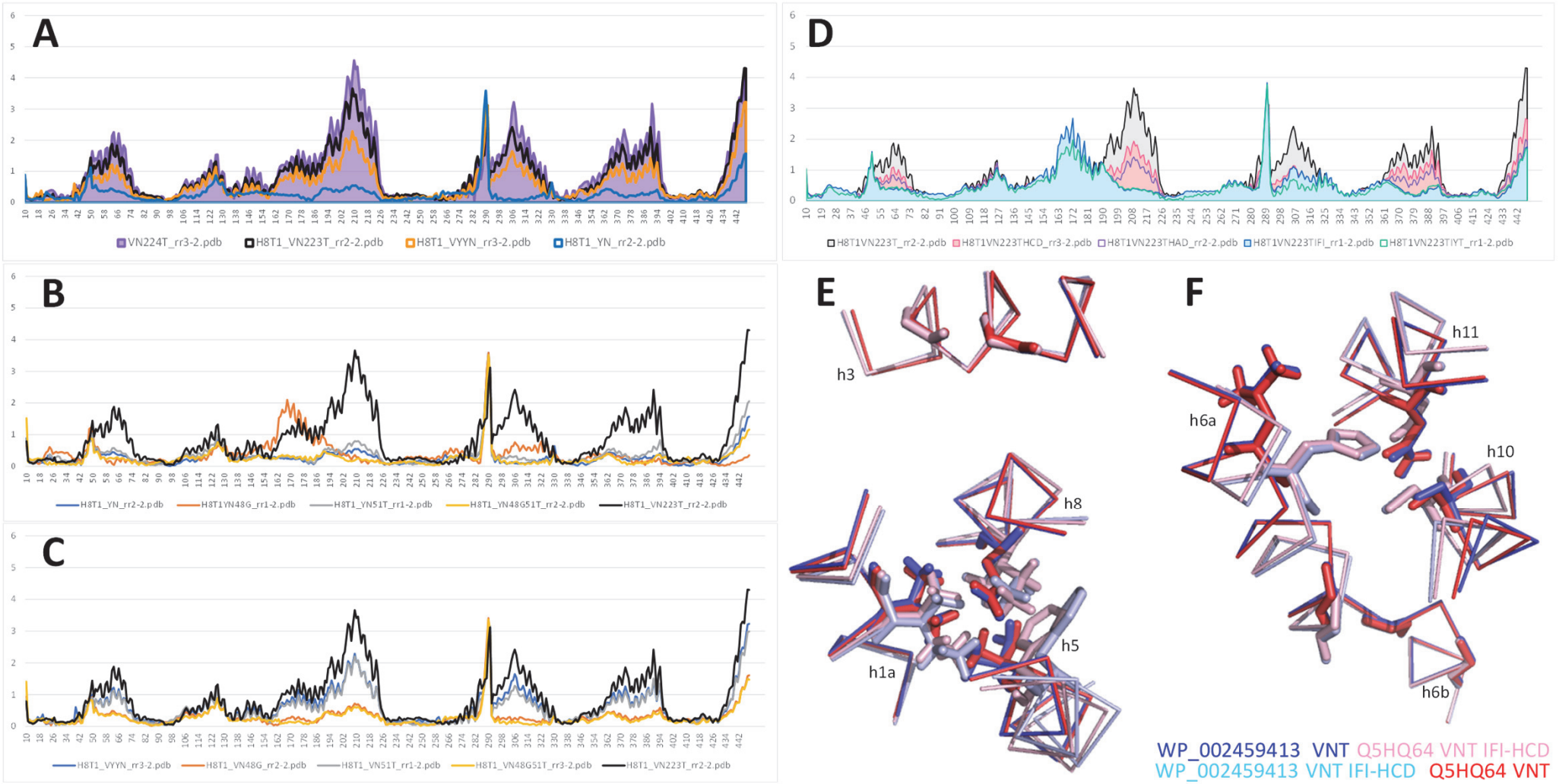

Figure S17. In silico mutagenesis of MCb gating communities prevents VNT-induced switch of CF pdb MCb models. **A-D**. Per residue RMSD from wt A0A380H8T1 or WP_002459413 IO conformer of models obtained for various mutants. **A**. Combined mutations inducing IO to OO conformation switch for both A0A380H8T1 and WP_002459413 (VNT, h3 YN h6 VY A223T). **B&C**. Combinations of A0A380H8T1 h1 mutations (D48G, N51T or both) with h3 YN background (**B**) or with h6 VY and h3 YN background (**C**). **D**. Separate targeting of either MCb 5M87 OO community c7 (IFI, h1a V50I, h5 V177F, h8 N334I and IYT, h1a V50I, h5 V177Y, h8 N334T) or MCb 5M94 IO community c11 [nc18] (HCD, h6a L223H, h10 S398C, h11 N442D and HSD, h6a L223H, h10 S398A, h11 N442D) in A0A380H8T1. **E&F**. Combined targeting of both OO community/inner gate (IFI) and IO community/inner gate (HCD) in WP_002459413. Superposed models obtained for VNT (dark color) and VNT IFI-HCD (light color) mutants of both WP_002459413 (blue) and Q5HQ64 (red).

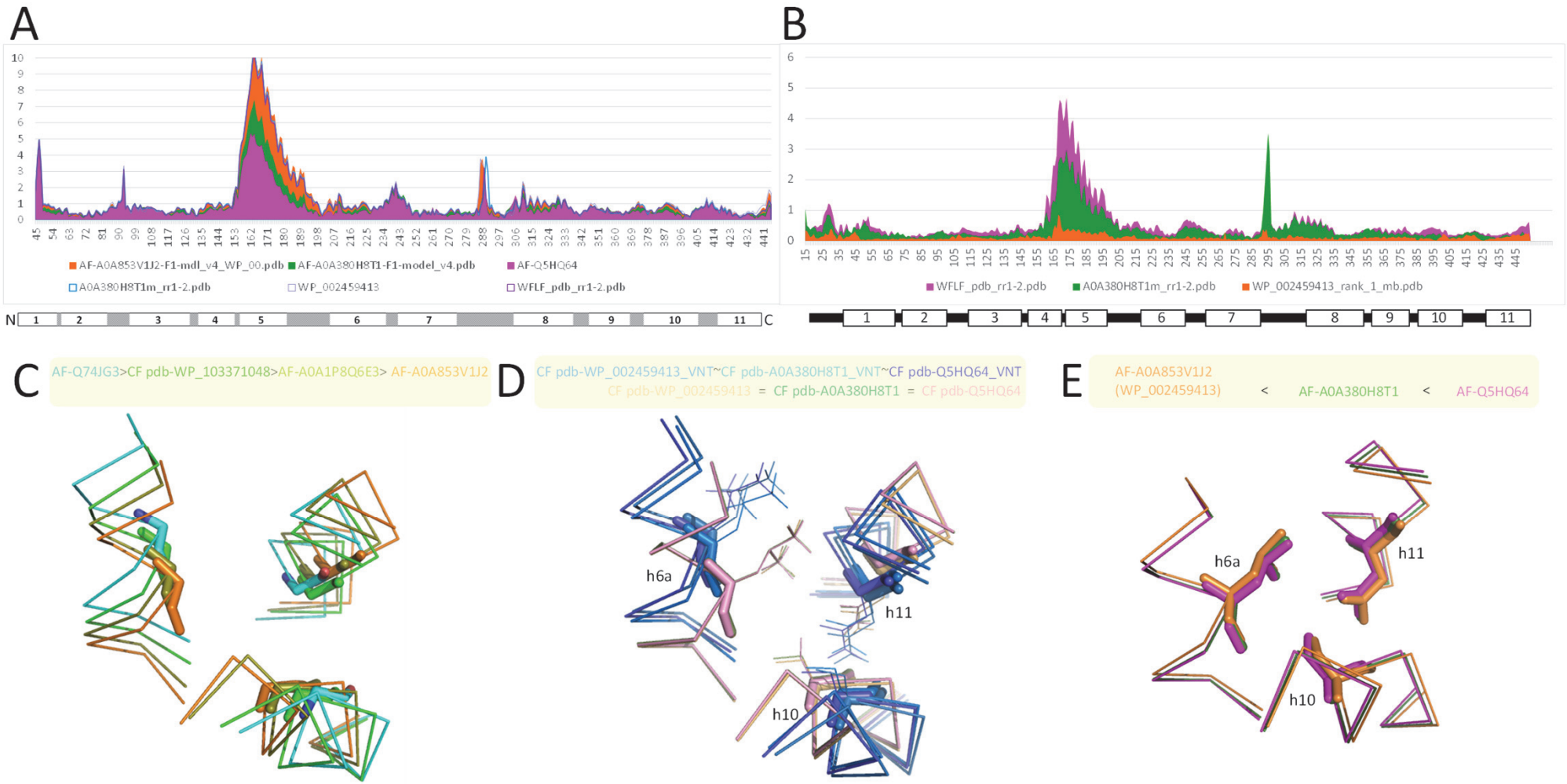

Figure S18. MCb transition from OO to IO comprises two successive processes distinguished by AF2 vs CF pdb modeling. A. *Per residue RMSD from MCb 5M94 IO structure of AF2 and CF pdb models for A0A853V1J2/WP_002459413, A0A380H8T1 and Q5HQ64).* ***B.*** *Respective per residue RMSD between pairs of AF2 and CF pdb models (A0A853V1J2/WP_002459413; A0A380H8T1; Q5HQ64).* ***C-I****. 3D superpositions showing evolution of local areas of MCb models during separate processes of OO carrier switch coupled to unlocking the inner gate (**C&G**), mimicked by the VNT mutation (**D&H**) vs inner gate motion leading to IO carrier (**E&I, F**). Accessions and corresponding color codes are indicated for each panel.*

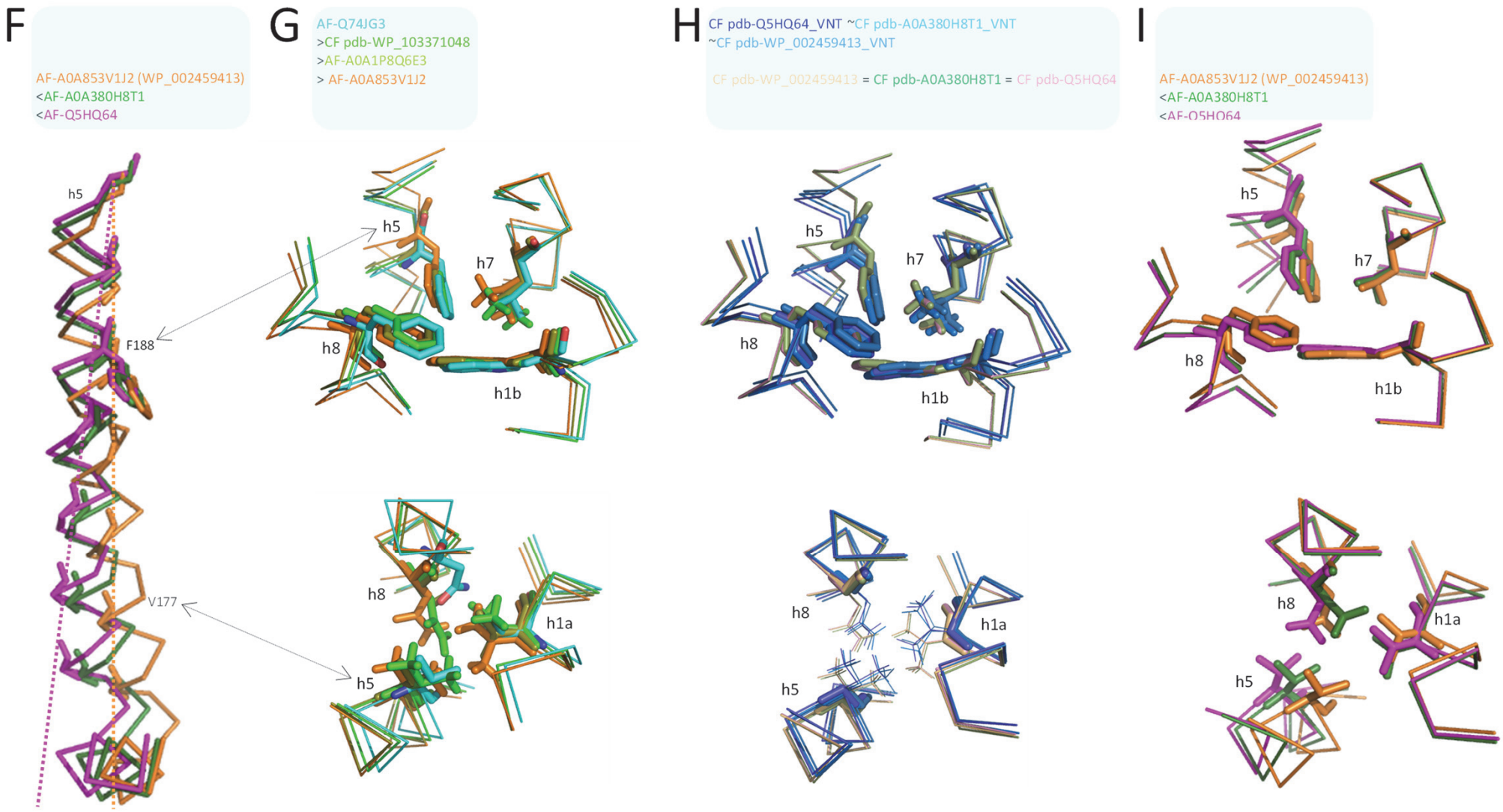

Figure S18 (contin'd).

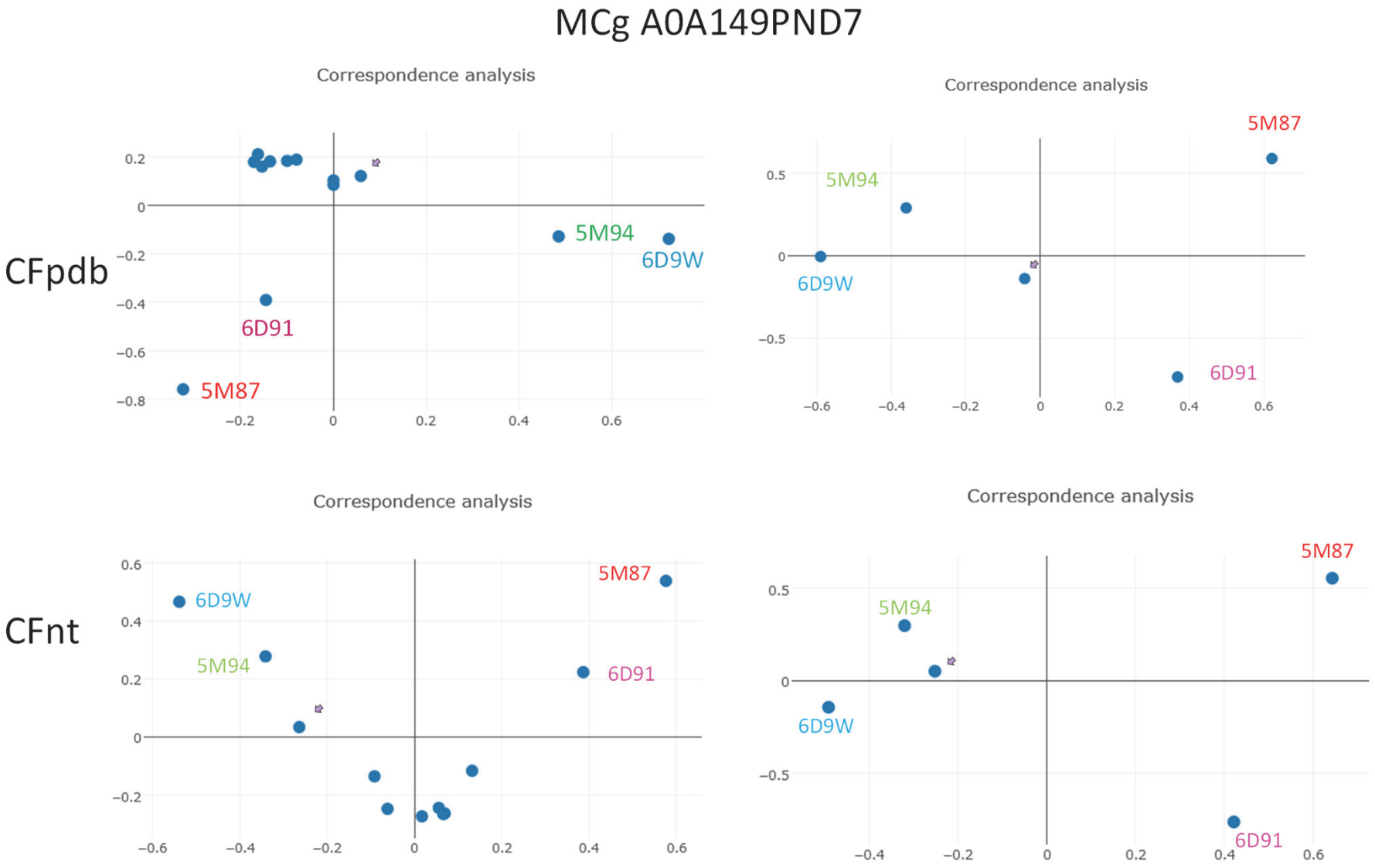

Figure S19. Structural variation among MCg models obtained with either CF with pdb template (CF pdb) or CF with no template (CF nt). *Left panel*. Pairwise comparisons (DALI All Against All) of wt MCg models, using MCb reference structures (5M87 and 5M94) and MA (6D91 and 6D9W) structures as outgroup. *Right panel*. Re-analyses of the models picked from left (red arrow) identify CFnt model of A0A149PND7 as candidate IO conformer.

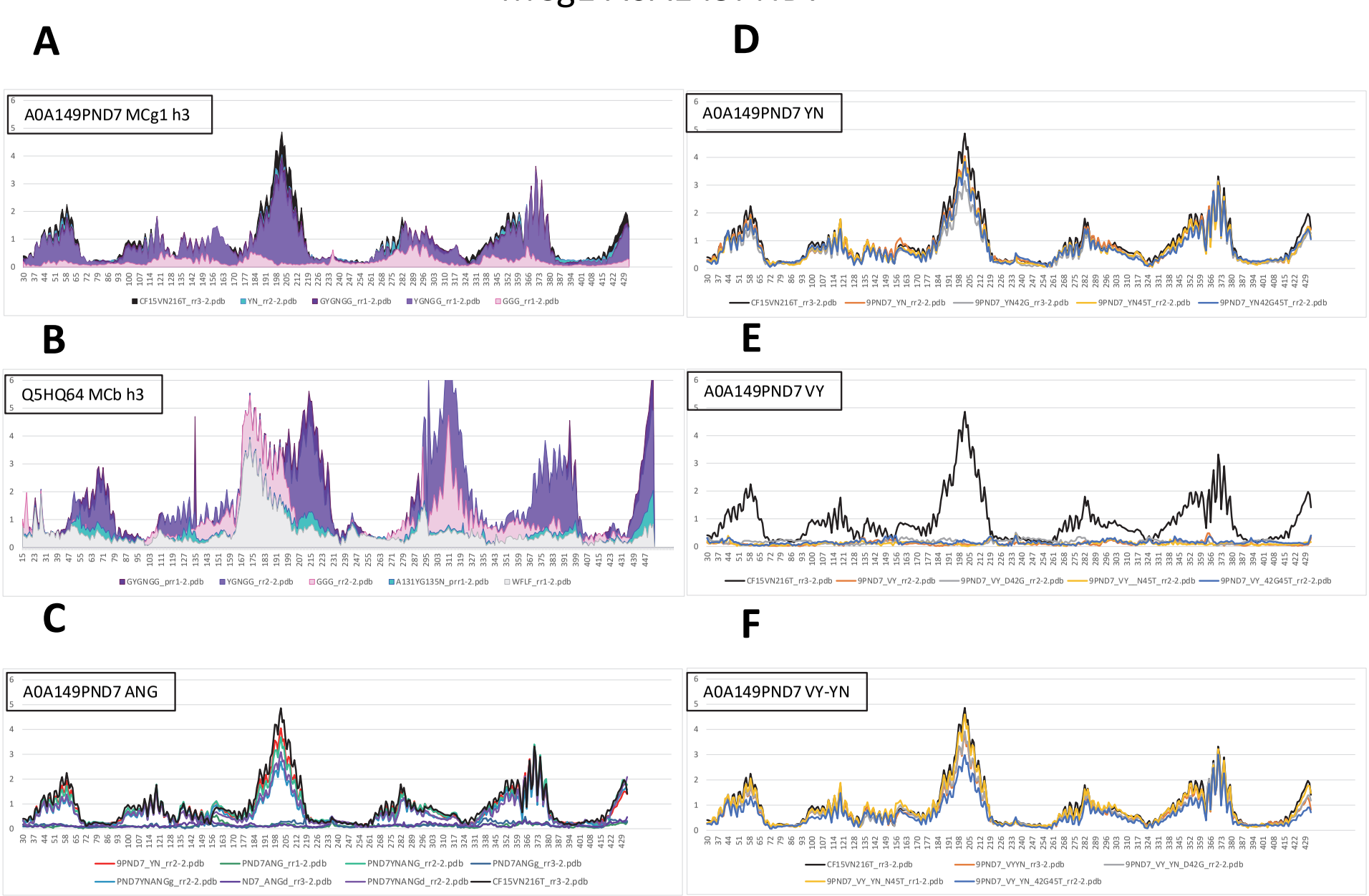

Figure S20. h3 YN mutation switching MCg1 A0A149PND7 IO conformation to OO state is modulated by other synapormorphic sites (h1, h6, h10 and h11). Per residue RMSD for models obtained using CF nt or CF pdb and aligned with either wt A0A149PND7 CF nt model (**A**, **C-F**) or wt Q5HQ64 CF pdb model (**B**), respectively. **A, B**. Compound mutants h3 GGG,YN, YGNGG, GYGNGG of MCg1 A0A149PND7 (**A**) and MCb Q5HQ64 (**B**). **C**. h10/h11 compound mutants ANG, YNANG, ANGg, YNANGg, ANGd, YNANGd. **D-F**. Mutation combinations of h3 YN (D), h6 VY (E) and h3 YN h6 VY (F) with h1 mutants D42G or N45T or both.

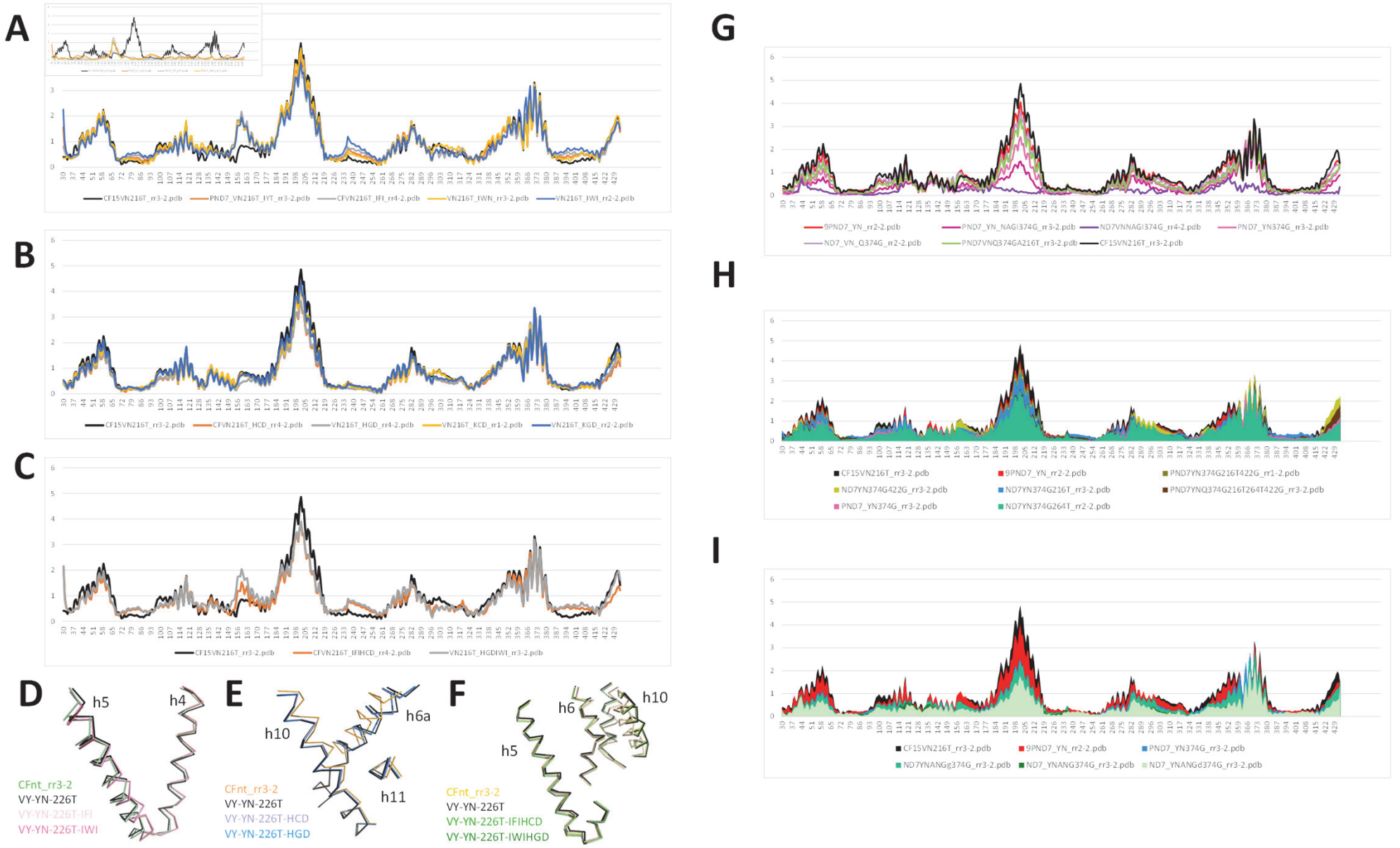

Figure S21. Structural divergence of MCg1 A0A149PND7 from MCbs. Per residue RMSD for models obtained using CF nt and aligned with wt MCg1 A0A149PND7 (CF nt) (**A-C**, **G-I**) are presented together with select Pymol Ca trace displays of POSA multiple alignment of MCg1 models (**D**, **F**, **H**). **A-C**. A0A149PND7 VNT mutant served to test the impact of mutations that prevented MCb IO to OO switch by altering carrier gating (outer gate, **A&D**, inner gate, **B&E,** both, **C&F)**. **G-I**. A0A149PND7 h10 Q374G mutation suppressing YN-induced conformation switch allows probing cooperation with synapomorphic sites located in h6 (**G**), h7 and h11 (**H**), h10 and h11 (**I**).

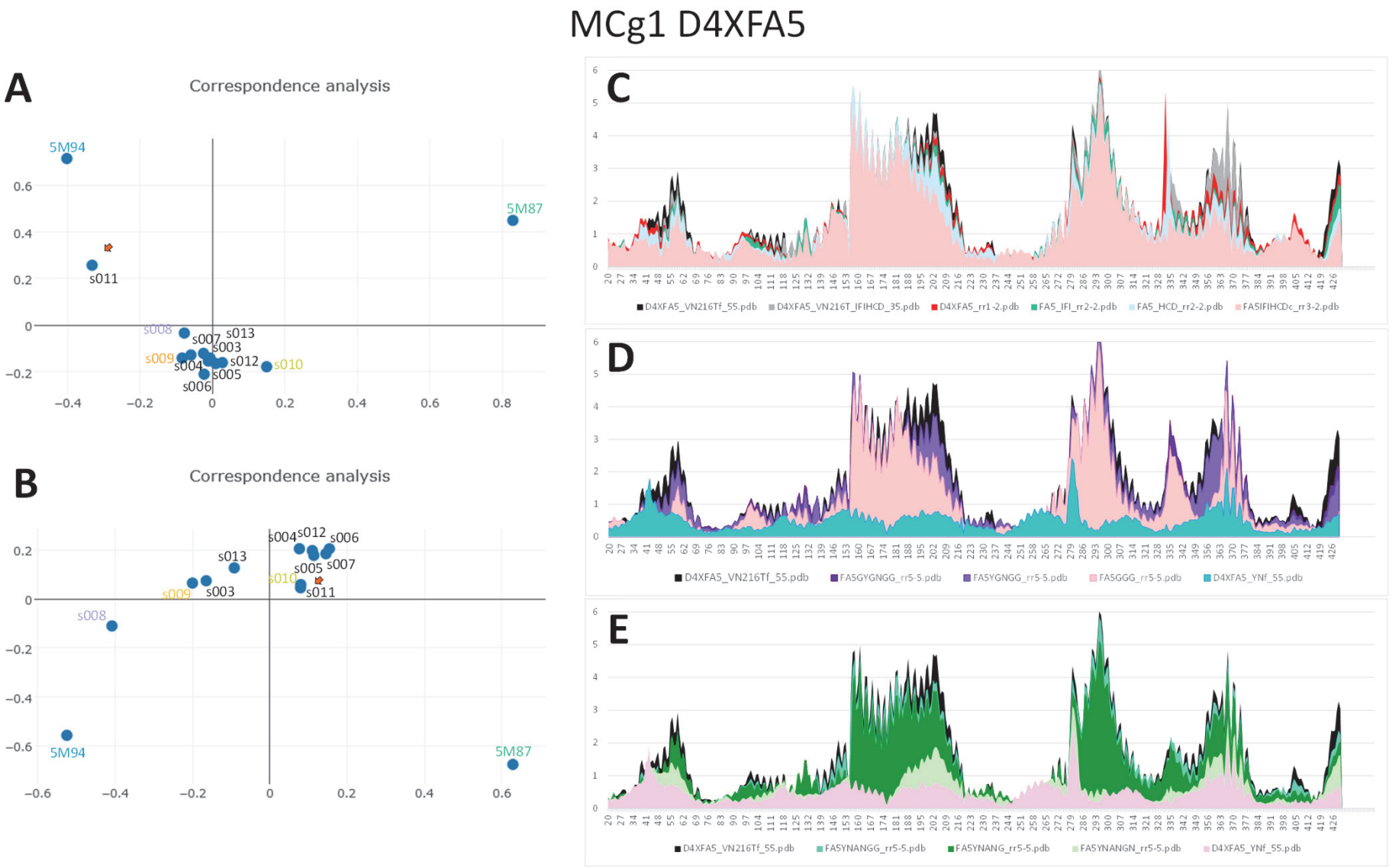

Figure S22. CFnt models candidate alternate conformers of MCg1 D4XFA5. Dali AAA-based re-examination of CF nt models obtained using AF2 training model5 (**A**) or AF2 training model2 (**B**) for MCg homologs (cf Figure 1 or Uniprot proxies) using as reference structures, MCg1 A0A149PND7 models (IO, aCF-rr1-2, s008/violet, and its converted OO form, A0A149PND7 VY-YN-216T CF nt-rr3-2, s010/lime) together with the pair of MCb structures OO (5M87) and IO (5M94) used as outgroup. The structure s009/orange is the actual prediction for native A0A149PND7 resulting from each CF nt run. **C-E**. Per residue RMSD of CF nt models for MCg1 D4XFA5 (wt CF nt rr3-5 used as reference IO model). **C**. D4XFA5 CF nt model rr1-2 is an OO state mimicked by CF nt model rr5-5 of D4XFA5 VNT mutant (h3 YN h6 VY A216T); it is also partially inhibited by mutations known to impair MCb carrier gating. **D**. D4XFA5 h3 mutagenesis suffices to switch IO to OO conformation but YN mutation is required to move selective segments (h1, h6, h10). **E**. D4XFA5 h11 site D422 modulates cooperation between h3 YN and h10 ANG mutations.

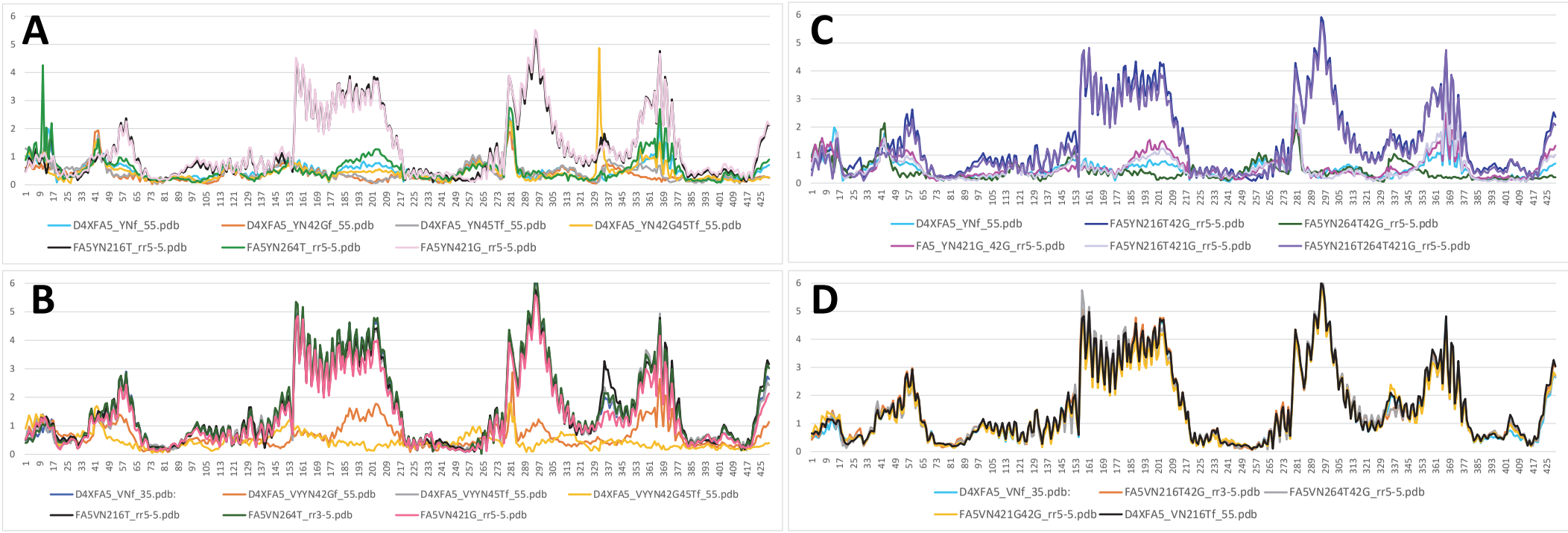

Figure S23. Influence of Slc11 synapomorphic site mutagenesis on MCg1 D4XFA5 conformation switch. Per residue RMSD of CFnt models for D4XFA5 mutants aligned with wt D4XFA5 CF nt rr3-5 used as reference IO structure (inner gate open) in h3 YN mutant background (**A&C**) or in h3 YN h6 VY mutant background (**B&D**). **A&B**. Effect of point mutations in h1 (D42G, N45T, 42G45T), h6 (A216T), h7 (N264T), h11 (D421G). **C&D**. Impact of h1 D42G mutation combined with h6 (A216T), h7 (N264T), h11 (D421G), and modulation of YN A216T D421G by N264T mutation (**C**).

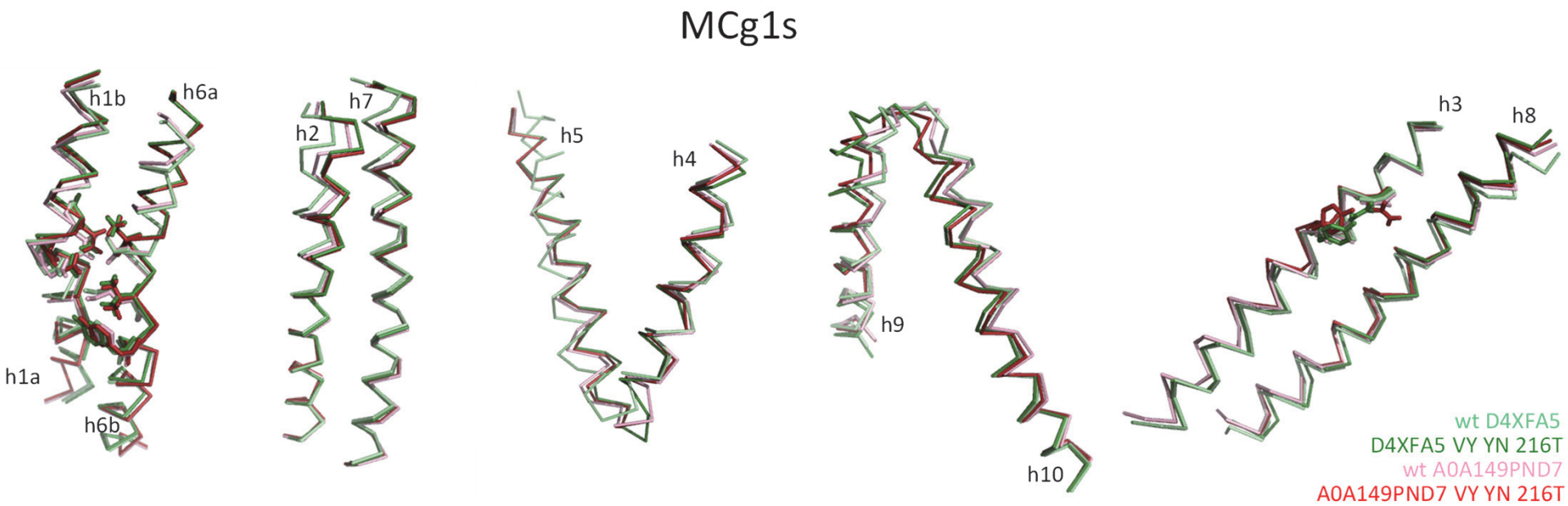

Figure S24. Similar switch of IO to OO conformers among divergent MCg1s. Two pairs of native MCg1 IO and VNT mutation-induced OO conformers (D4XFA5 and A0A149PND7) were superposed and Ca trace deviations are presented separately for either adjacent or linked helices. Sticks indicate residues forming the substrate binding site (h1 & h6) and the conformation-driving mutation h3 YN.

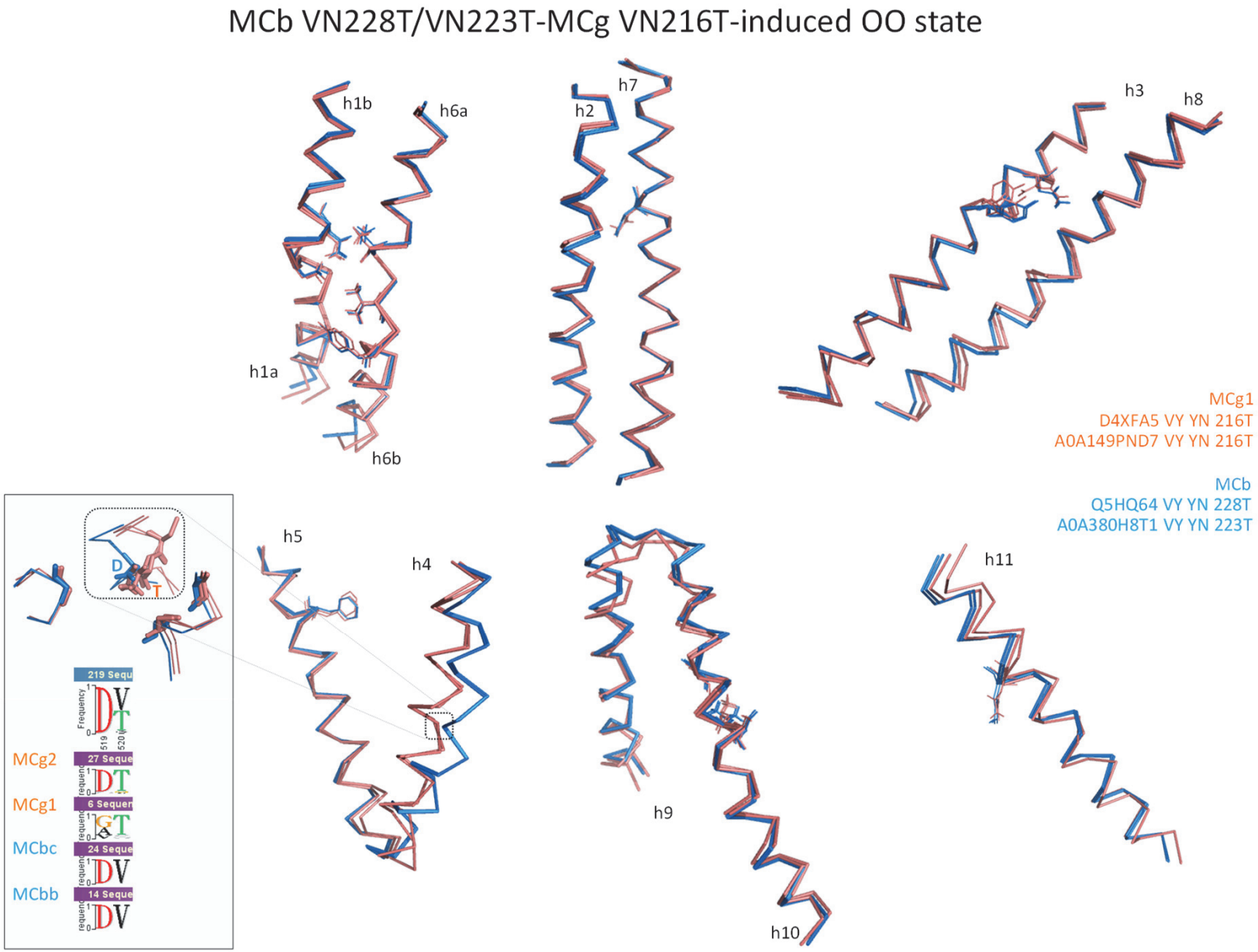

Figure S25. 3D arrangement of Slc11 synapomorphy is conserved among MCbs and MCg1s. 3D superposition of VNT mutation-induced OO states for pairs of MCb and MCg1 models. Slc11 synapomorphic sites are highlighted by representing side chains with lines (h1, h3, h6, h7, h10, h11) together with h5 putative pivot point. *Inset*. Details of MCg1 h4 sequence divergence and 3D rearrangement of the H^+-network.

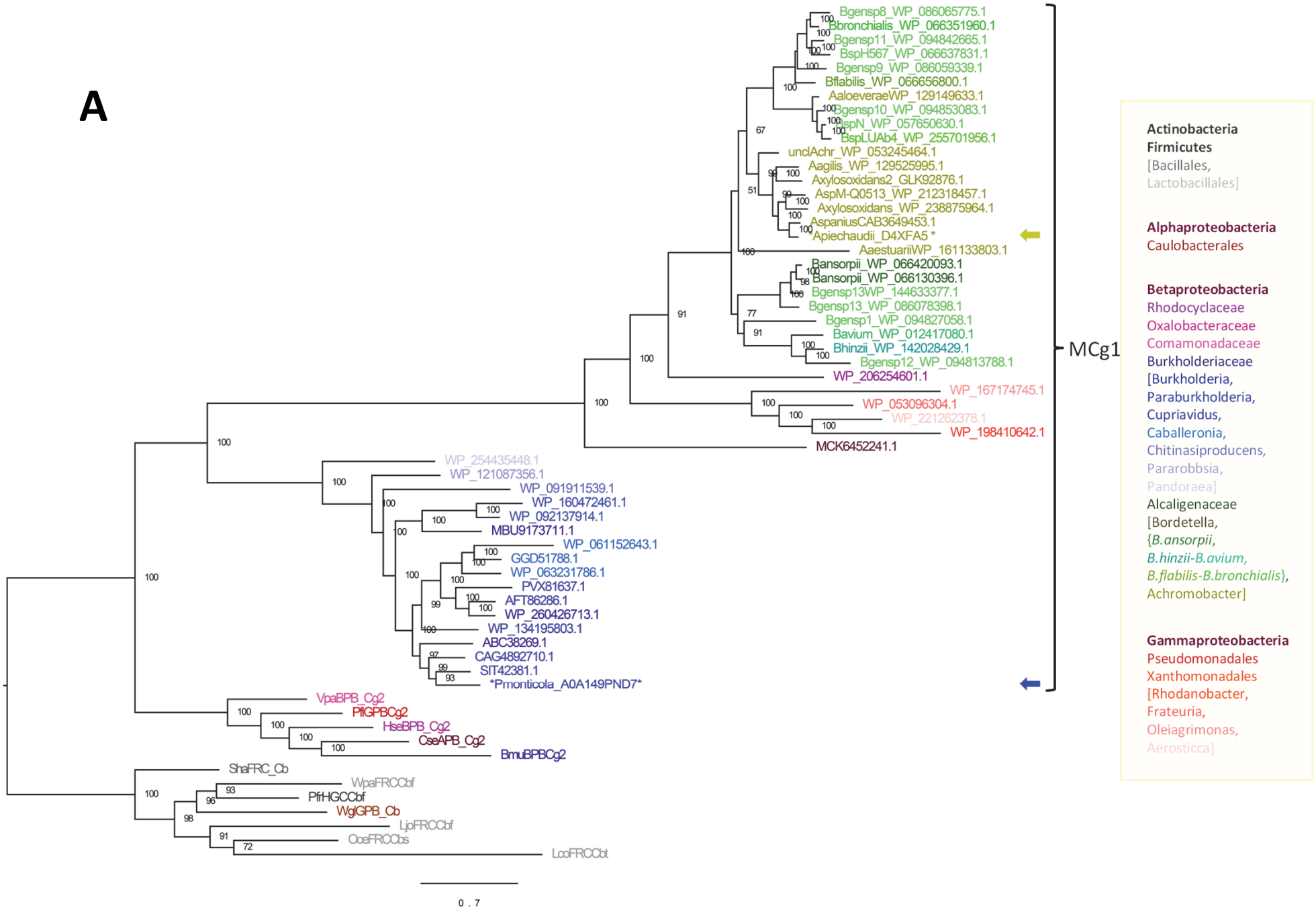

Figure S26. Phylogeny of MCg1. The IQ-trees presented were calculated using parsimony informative (PI) sites, the substitution mixture model EX-EHO, ML estimate of a.a. state frequency, free rate model of variation among sites with 10 (**A**) or 8 (**B**) categories. Also, 1000 replica of each of two types of branch support calculations (ultrafast bootstrap and SH-aLRT single branch test) were performed to estimate confidence in the tree clades obtained. A scale bar representing the number of substitutions per site is provided. **A.** IQ-Tree using 343 PI sites representing 61 seqs, including 32 seqs ("D4XFA5 MCg1 cluster"), 17 seqs ("A0A149PND7 MCg1 cluster"), 5 MCg2 seqs and seven MCb seqs, the latter being used to root the tree. The taxonomic distribution of the sequence encoding genomes is color-coded. The relative positions of D4XFA5 and A0A149PND7 in MCg1 phylogeny are indicated with arrows.

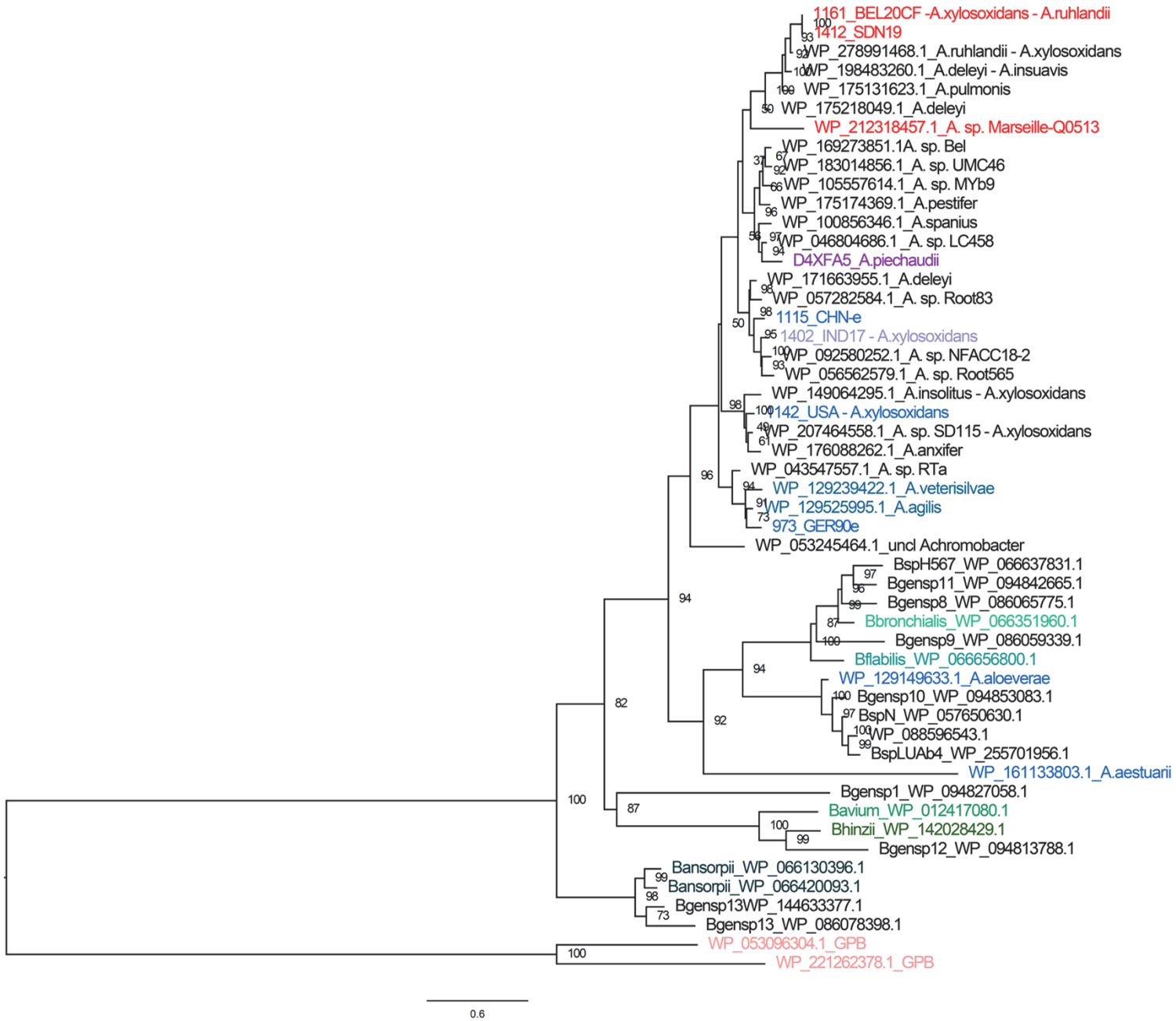

Figure S26. Phylogeny of MCg1. **B.** IQ-Tree using 248 PI sites representing 51 seqs from D4XFA5 MCg1 cluster. Some of the most divergent seqs from this cluster (from GPB, cf A.) were used to root the tree (highlighted with salmon color). Seqs encoded by *Bordetella* spp. are indicated with green tints (*B. ansorpii; B. hinzi* & *B. avium*; *B. flabilis* & *B. bronchialis*). Different colors distinguish *Achromobacter* spp. of environmental origin (blue to violet tints) from those isolated from patients (red), including six reference strains from the PubMLST collection (1161_BEL20CF, 1412_SDN19, 1115_CHN-e, 1402_IND17, 1142_USA, 973_GER90e). The *Achromobacter* seqs used represent clusters (95% id, 13 singletons). One representative spp. name is provided; additional presence per cluster of isolates from either *A. xylosoxidans*, *A. ruhlandii* or *A. insuavis* is also indicated (potential emerging pathogens in patients with cystic fibrosis, CF).

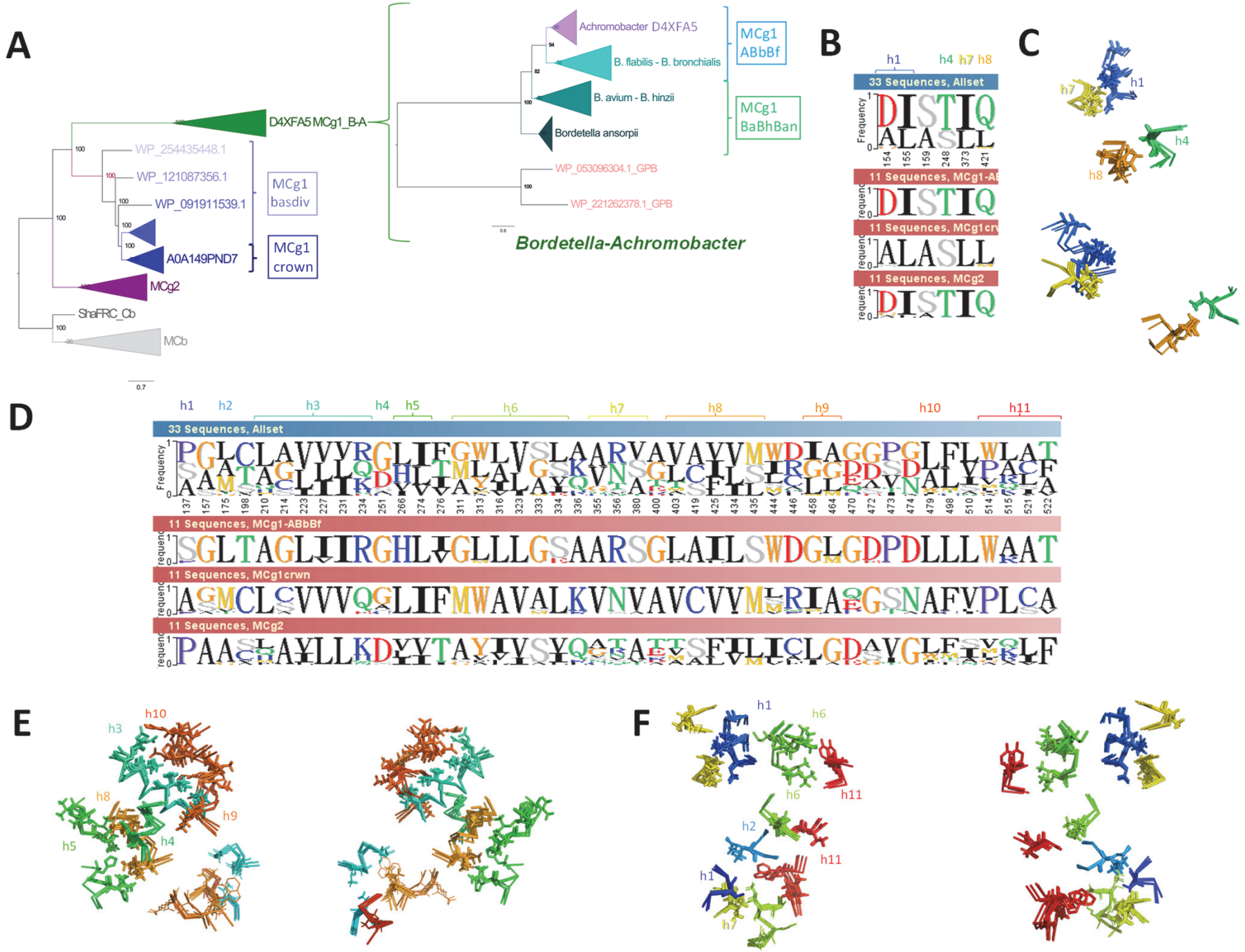

Figure S27. Divergence of the clusters represented by A0A149PND7 (MCg1 crown) and D4XFA5 (MCg1 ABbBf/*Bordetella-Achromobacter*) shows 3D colocalization of evolutionary coupled mutations. **A.** Simplified MCg1 phylogeny detailing the 3 groups of sequences that were analyzed (MCg2, MCg1 crown, and MCg1 ABbB. **B&D**. Phylo-logo displays of two classes of divergent sites that were examined: sites conserved between MCg2 and MCg1 ABbB but distinct in MCg1 crown (**B**), group-selective sites (**D**). Transmembrane site helix location (h1-h11) are indicated above. **C, E&F**. 3D mapping of the divergent sites presented in B (**C**) and D (**E&F**), using the superposed models shown Figure S25. **E**. Helices 3, 4, 5, 8, 9, 10. **F**. Helices 1, 2, 6, 7, 11. Two views are presented per panel.

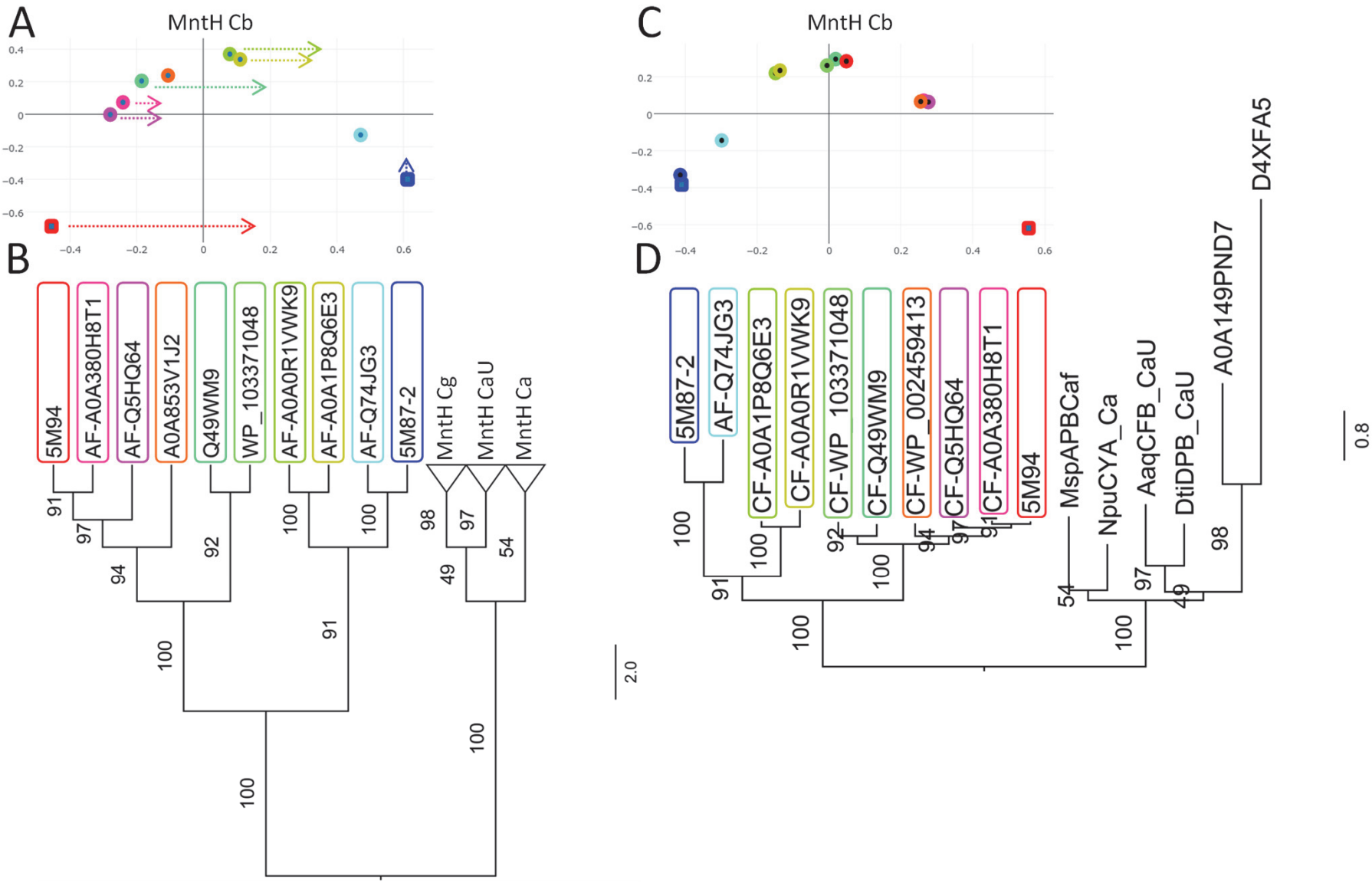

Figure S28. AF2 and CF pdb modeling of MCbs show strong phylogenetic component. A,C. 3D relationships of models obtained for MCb sequences (dots) using AF2 (**A**) or CF pdb (**B**) and MCb reference structures (squares). Sequence relationships were established with IQ-Tree (306 PI sites) using as outgroup sequences from other MC groups, and are represented either as a cladogram (**C**) or a dendrogram showing genetic distances (**D**). MCb sequences are color-coded to highlight four monophyletic clusters. Dotted arrows (**A**) indicate sequences that yield distinct conformers using AF2 or CF pdb modeling.

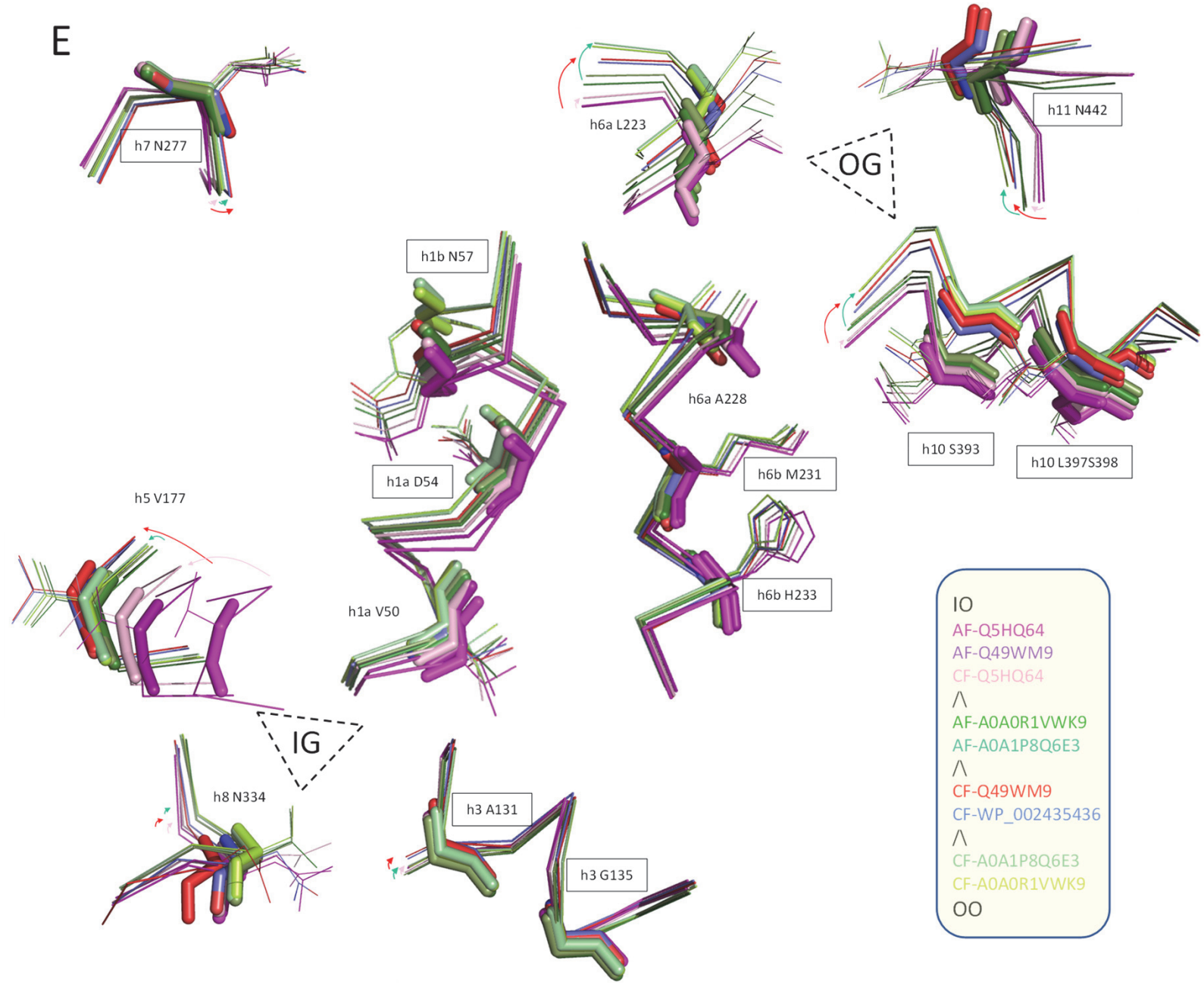

Figure S28 (contin'd). AF2 and CF pdb modeling of MCb show strong phylogenetic component. E. 3D superposition of the models listed as sequential intermediates spanning MCb carrier transition from OO to IO, based on panels A&B with color change for Q49WM9 and WP_002435436. The residues shown are represented as stick (main chain) and line (side chain, no H) and colored as per model. The residues forming Slc11 synapomorphy are boxed; other residues presented contribute to outer or inner gating (h6a and h1a, h5, h8, respectively) as part of networked communities schematized as dotted triangles. Colored arrows indicate main chain displacement between respective AF2 and CF pdb models.